Design of advanced one-step hydroxyapatite coatings for biomedical applications using the electrostatic spray deposition

Verónica Müller, Thierry Pagnier, Solene Tadier, Laurent Gremillard, Matías Jobbagy, Elisabeth Djurado

Design of advanced one-step hydroxyapatite coatings for biomedical applications using the electrostatic spray deposition

Published in Applied Surface Science, 2021 vol. 541, article # 148462,
https://doi.org/10.1016/j.apsusc.2020.148462

Verónica Müller[a,b], Thierry Pagnier[a], Solène Tadier[b], Laurent Gremillard[b], Matías Jobbagy[c], and Elisabeth Djurado[a*]

[a] Univ. Grenoble Alpes, Univ. Savoie Mont Blanc, CNRS, Grenoble INP, LEPMI, 38000 Grenoble, France
[b] Univ. Lyon, INSA Lyon, UCB Lyon 1, CNRS, MATEIS UMR 5510, 69621 Villeurbanne, France
[c] Univ. Buenos Aires, Facultad de Ciencias Exactas y Naturales, INQUIMAE-DQIAQF, C1428EHA Buenos Aires, Argentina

Corresponding author: Elisabeth Djurado
E-mail: elisabeth.djurado@lepmi.grenoble-inp.fr, Tel: +33-476826684; Fax: +33-476826777

Keywords
calcium phosphate; hydroxyapatite coatings; electrostatic spray deposition; metallic dental implant; Ti6Al4V substrate.

Abstract
Calcium phosphate ceramics (CaP), particularly hydroxyapatite $Ca_{10}(PO_4)_6(OH)_2$ (HAP), are widely used as surface coatings on top of titanium and its alloys in biomedical applications thanks to their ability to form strong bonds with natural bone tissues. In this paper, the electrostatic spray deposition technique (ESD) by using an organic phosphorus (V) precursor is proposed as an alternative to the widely used plasma-spraying process. This bottom-up approach enables the one-step fabrication of single-phase crystalline HAP coatings with unique morphologies. The microstructure and composition of the deposited CaP layers result from a delicate compromise between the physicochemical properties of the precursor solution and the ESD deposition conditions. An in-depth study of their structural, microstructural, compositional properties and their reactivity with Ti6Al4V is undertaken. It shows that the Ca/P molar ratio and the nature of phases are strongly dependent on hydrolysis and evaporation of the P(V) precursor in the ESD process. Optimized deposition conditions are found by using solvents of low-boiling point, for which the coatings deposited above 325 °C correspond to a well crystalline, nanostructured, and single-phase HAP. Infrared heat treatment of a coating prepared from the one optimized precursor solution promotes nanostructured HAP.

1. Introduction

Calcium phosphate-based (CaP) coatings on metallic implant substrates are known to improve bone strength and initial osseointegration rate [1–6]. Most CaP materials are categorized as bioactive ceramics, exhibiting high biocompatibility and bioactivity in contact with bone cells and building a direct chemical connection between bone tissues and ceramic-coated implants [7,8]. Among these CaP ceramics, hydroxyapatite ($Ca_{10}(PO_4)_6(OH)_2$, HAP) stands as a leading biomaterial because of its chemical resemblance with the inorganic component of human bone [9,10]. Great attention has been driven onto calcium phosphate coatings to improve the biological integration of Ti-based implants. Titanium and its alloys are the most commonly used materials for load-bearing medical devices due to their low density, high strength, and excellent corrosion resistance, among other properties, while CaP ceramics are well known to be brittle. So, Ti-based implants coated with CaP are an excellent approach to combine the mechanical strength of titanium with the biological properties of calcium phosphates.
Currently, plasma spraying or arc plasma-spraying is the most widely applied technique, and the only U.S. Food and Drug Administration-approved one, for depositing a calcium phosphate coating on implant surfaces [11,12]. The advantages of plasma spraying lie in its inherent rapid deposition rate and its relatively low cost [13]. However, serious shortcomings mainly related to the extremely high processing temperatures and rapid cooling rate of this technique result in unpredictable phase transitions [14,15]. HAP powder may be partially decomposed under the plasma flame to form dehydroxylated CaP phases like tricalcium phosphate [$Ca_3(PO_4)_2$, TCP], tetracalcium phosphate [$Ca_4(PO_4)_2O$, TTCP], partially dehydrated hydroxyapatite, and even calcium oxide (CaO) [16,17]. In addition, the impact of molten HAP powder onto the metal substrate produces an amorphous calcium phosphate (ACP) layer at the interface, which may result in poor adhesion between the coating and the metallic implant [18]. Therefore, plasma spraying of pure crystalline HAP coatings, free of secondary phases, is exceedingly difficult. Moreover, to completely cover the implant, plasma-sprayed coatings are rather thick, between 50 and 200 µm [19,20]. These excessively thick coatings result in high fatigue and shear stresses, increasing the risk of implant failure due to cracks within the coating or coating chipping [21,22].

In light of the deficiencies of plasma spraying, alternative techniques are being developed for depositing thin HAP-based coatings, including sol-gel deposition [23], dip coating, electrochemical deposition [24,25], RF magnetron sputtering deposition [26,27], Pulsed Laser Deposition (PLD) [28] and Hot Isostatic Pressing (HIP) [29,30]. Among these methods, the Electrostatic Spray Deposition technique (ESD) has been reported as a promising low-temperature deposition technique for producing CaP coatings [31–37], which may eliminate some of the problems associated with the plasma-spraying process. The preparation of CaP coatings by ESD has been reported using H_3PO_4 as a P(V) precursor [31-33]. Amorphous as-deposited CaP coatings were obtained, but additional heat treatment was required for improving the mechanical properties of the coatings [33]. ESD has also been used to shape HAP coatings from spraying a suspension based on HAP nanostructured powders [34–37]. However, this procedure although in one step has drawbacks, such as the instability of the suspension, compositional homogeneity, and thus the reproducibility of the deposition. Besides, the use of HAP nanoparticles in the ESD process limits the fine-tailoring of coating's microstructure.

ESD is a low-cost chemical method since it does not require expensive equipment or vacuum generation. Furthermore, it presents a high coverage rate, allowing the use of small amounts of precursors. It is an innovative technique that enables the deposition of films with a large variety of original morphologies with a nano-texturing approach depending on process conditions. ESD has been reported to be used in depositing a large variety of oxide materials [38] while ensuring strong adhesion to the substrate. Moreover, this technique allows for excellent control over the stoichiometry and the thickness of the films. It is expected that thin films will be advantageous in the sense that less material will be necessary,

and the residual stresses expected at the metal-ceramic interface should be reduced, improving the mechanical performance of the coated implant.

The microstructure of ESD deposited films depends mainly on the size of the droplets impacting the heated substrate. According to Gañan-Calvo's equation (Eq. 1) [39], the droplet size at the tip of the needle (D, μm) can be estimated from the solution properties (ρ, the solvent density [40], γ, the surface tension [40], and K, the electrical conductivity), with Q being the precursor solution flow rate and ε_0 the vacuum permittivity (8.85×10^{-12} F·m^{-1}) (Table 1).

$$D \sim \left(\frac{\rho \varepsilon_0 Q^3}{\gamma K} \right)^{1/6} \qquad \text{(Equation 1)}$$

The control of droplet sizes impacting the substrate is also strongly dependent on other ESD deposition parameters such as the substrate temperature (T), the nozzle-to-substrate distance (d), and the deposition time (t) [41,42]. On the other hand, the chemical composition of the coatings is determined by the physicochemical properties of the precursor solution, including the solvent and the nature of precursors. In this paper, we present a robust method for the preparation of crystalline single-phase hydroxyapatite coatings by using triethyl phosphate (TEP) or O=P-(O-CH_2-CH_3)$_3$ as the P(V) precursor and calcium nitrate as a Ca(II) precursor. For the first time, an organic P(V) precursor solution has been used in the ESD process. The main advantage of using TEP instead of inorganic P(V) precursors, e.g. H_3PO_4 in previously reported works [31], is its ability to be dissolved in several solvents at high concentration, in the presence of free calcium ions and at any pH, and Ca/P ratios can be varied without risk of early precipitation of undesirable CaP phases in the precursor solution. The originality of this chemical approach relates to the deposition of a pure HAP film in a single-step fabrication process. The TEP precursor allows a bottom-up approach for obtaining crystalline HAP coatings with controlled grain size and unique morphologies from dense to highly porous films. However, due to the alkoxide nature of TEP, the effective incorporation of P(V) in the final coatings is strongly conditioned by the competition between hydrolysis of TEP and its evaporation during the deposition process. Considering the properties of TEP and the ESD parameters that may control the final coating, several precursor solutions and deposition parameters were tested to understand the behavior of this P(V) precursor in the ESD process and to achieve the deposition of single-phase HAP coatings. Furthermore, structural changes of coatings associated with two different post-deposition heat-treatments (conventional heat treatment in a furnace and fast heat treatment under an infrared lamp) have been investigated.

2. Material and methods

2.1 ESD process

Briefly, the ESD process [38] is based on electrohydrodynamic laws where a precursor solution is pumped through a metallic nozzle at a controlled flow rate. A positive high voltage is applied to the stainless-steel nozzle from which positively charged droplets are generated and directed to the grounded substrate. When the electric field is strong enough, the electrostatically stressed liquid surface can be distorted into a stable conical shape (Taylor cone) characterized by mono-sized droplets in the range of micrometers [42,43]. Following the impact of the droplets onto the heated substrate, a series of events including spreading, decomposing, and drying occur more or less at the same time to form a thin layer.
A home-made, vertical ESD set-up was used to deposit CaP/HAP coatings on polished commercial Ti6Al4V ELI plates (ACNIS-Titanium). Substrates were brought to a mirror-finish surface, as the last step of polishing, using the suspension (OP-S, 0.25 μm (Struers) with 30 wt. % hydrogen peroxide

(Merck) (75:25)) on a ChemoMet polishing cloth (Buehler) for 30 min. Then they were cleaned ultrasonically in acetone (15 min), ethanol (15 min), and distilled water (10 min) before deposition. A positive high voltage was applied between the needle (tilted outlet stainless steel nozzle, 3 cm long and 0.6 mm inner diameter, STERICAN® - B. Braun) and the grounded substrate to generate a spray of positive micro-sized charged droplets. High voltage values ranging from 6 to 12 kV were used for spraying under a stable cone-jet mode. The precursor solutions were delivered to the nozzle by a syringe pump (KD Scientific), and the flow rate was fixed at 1.5 ml h^{-1}. Substrate temperatures, controlled by the voltage applied to the heating element, were chosen in the range of 300-400 °C. The nozzle-to-substrate distance and deposition time remained fixed at 30 mm and 1.5 h, respectively.

2.2 Precursor solutions

Several solutions, with variable Ca/P molar ratios and absolute precursor concentrations, were prepared by mixing calcium nitrate $Ca(NO_3)_2.4H_2O$ (Merck, 99.95%) and triethyl phosphate (TEP, Sigma-Aldrich, 99.8%) into various solvents chosen based on their different boiling points and chemical nature (Table 1). Working solutions were prepared by adding an adequate amount of pure TEP in a previous Ca(II) based-solution. The conductivity of the solutions was measured with a CDRV 62 conductimeter at 25 °C.

The effect of the P(V) precursor concentration on the composition of coatings was investigated by keeping the $Ca(NO_3)_2$ concentration constant at 15 mM, and varying the TEP concentration from 9 mM to 75 mM. In the following, these solutions will be referred to as SL and their corresponding coatings to as L (L: from A to H). In addition, the TEP behavior under electrospraying was analyzed by studying the influence of several deposition parameters, such as water content in the precursor solution, solvent boiling point, and substrate temperature (Table 1).

Table 1. ESD process parameters employed in this work: TEP nominal concentration, nature of the solvent(s), applied potential between needle and substrate (V), the estimated boiling point (b.p.) of the precursor solution, substrate temperature (T), estimated initial droplet size at the tip of the needle (D) from Eq. 1, nominal Ca/P ratio of precursor solutions, and Ca/P molar ratio of the deposited coatings as measured by EDS. The nominal concentration of $Ca(NO_3)_2$ was 15 mM for all solutions. Deposition time (t) was fixed at 1.5 h, needle-to-substrate distance (d) at 30 mm, and flow rate (Q) at 1.5 mL h^{-1}. The values of b.p, density (ρ), and surface tension (γ) of the solutions were estimated from a weighted average of the properties of the solvents from [40]

TEP (mM)	Nature of solvent(s)	V (kV)	b.p. (°C)	T (°C)	D (µm)	Nominal Ca/P ratio	Ca/P by EDS
9	MetOH	6 – 7	65	300	2.6	1.67	4.9 ± 0.2
9	MetOH	6 – 7	65	350	2.6	1.67	2.1 ± 0.1
9	EtOH	6 – 7	78	300	3.5	1.67	6.4 ± 0.7
18.75	EtOH	6 – 7	78	300	3.5	0.8	5.0 ± 0.2
9	EtOH	6 – 7	78	325	3.5	1.67	3.3 ± 0.2
18.75	EtOH	6 – 7	78	325	3.5	0.8	1.9 ± 0.1
9	EtOH	6 – 7	78	350	3.5	1.67	3.0 ± 0.1
10	EtOH	6 – 7	78	350	3.5	1.5	2.7 ± 0.1
12.5	EtOH	6 – 7	78	350	3.5	1.2	2.2 ± 0.1
15	EtOH	6 – 7	78	350	3.5	1	2.1 ± 0.1
18.75	EtOH	6 – 7	78	350	3.5	0.8	1.9 ± 0.1
25	EtOH	6 – 7	78	350	3.4	0.6	1.9 ± 0.1
37.5	EtOH	6 – 7	78	350	3.4	0.4	1.9 ± 0.1
75	EtOH	6 – 7	78	350	3.4	0.2	1.9 ± 0.1
9	EtOH	6 – 7	78	375	3.5	1.67	2.9 ± 0.1
18.75	EtOH	6 – 7	78	375	3.5	0.8	1.9 ± 0.1
9	EtOH	6 – 7	78	400	3.5	1.67	3.1 ± 0.1
18.75	EtOH	6 – 7	78	400	3.5	0.8	1.9 ± 0.1
9	EtOH: H_2O (19:1)	6 – 7	79	300	3.0	1.67	5.5 ± 0.7

9	EtOH: H_2O (19:1)	6 – 7	79	350	3.0	1.67	2.2 ± 0.1
9	EtOH: H_2O (19:1) + 2 mM NH_3	6 – 7	79	300	2.9	1.67	6.4 ± 0.7
9	EtOH: H_2O (19:1) + 2 mM NH_3	6 – 7	79	350	2.9	1.67	2.2 ± 0.1
9	EtOH: H_2O (19:1) + 2 mM HNO_3	6 – 7	79	300	2.9	1.67	6.4 ± 0.7
9	EtOH: H_2O (19:1) + 2 mM HNO_3	6 – 7	79	350	2.9	1.67	2.5 ± 0.1
9	EtOH: H_2O (19:1) - aged	6 – 7	79	350	3.0	1.67	2.2 ± 0.1
9	EtOH: H_2O (19:1) + 2 mM NH_3 - aged	6 – 7	79	350	2.9	1.67	2.1 ± 0.1
9	EtOH: H_2O (19:1) + 2 mM HNO_3 - aged	6 – 7	79	350	2.9	1.67	2.2 ± 0.1
9	EtOH: EG (19:1)	6 – 7	84	350	3.0	1.67	32 ± 4
9	EtOH: H_2O: EG (18:1:1)	6 – 7	85	350	2.8	1.67	21 ± 2
9	EtOH: H_2O (1:1)	12	89	300	2.2	1.67	2.9 ± 0.1
9	EtOH: H_2O (1:1)	12	89	350	2.2	1.67	2.5 ± 0.1
9	ButOH	6 – 7	118	300	5.3	1.67	8.4 ± 0.3
9	ButOH	6 – 7	118	350	5.3	1.67	3.3 ± 0.1
9	EG: EtOH (1:1)	9 – 11	138	300	3.0	1.67	P < D.T.*
9	EG: EtOH (1:1)	9 – 11	138	350	3.0	1.67	P < D.T.*
9	BC: EtOH (1:1)	7 – 8	155	300	3.7	1.67	P < D.T.*
9	BC: EtOH (1:1)	7 – 8	155	350	3.7	1.67	P < D.T.*
9	BC: H_2O (1:1)	12 – 13	166	300	2.5	1.67	P < D.T.*
9	BC: H_2O (1:1)	12 – 13	166	350	2.5	1.67	P < D.T.*
9	EG	11	198	300	3.3	1.67	P < D.T.*
9	EG	11	198	350	3.3	1.67	P < D.T.*
9	BC	6 – 7	231	300	5.6	1.67	P < D.T.*
9	BC	6 – 7	231	300	5.6	1.67	P < D.T.*

Abbreviations: MetOH: Methanol; EtOH: Ethanol; ButOH: 1-Butanol; EG: Ethylene glycol; BC: Butyl carbitol; H_2O: milli-Q® water.
* D.T. = detection threshold

2.3 Characterization of the ESD-coating

The microstructure and composition of the ESD films (as-deposited and heat-treated) were studied using scanning electron microscopy (SEM) with a field emission gun, FEG-SEM, (ZEISS GeminiSEM 500) coupled with an EDS probe (EDAX®), operating at 5 kV and 6 mm working distance for image analysis and 10 kV and 10 mm working distance for chemical analysis. The particle size of the CaP coatings was estimated from the SEM images using an image analysis tool (Image J® software). EDS allowed the estimation of the Ca/P molar ratio, each coating was analyzed in 5 spots (one in the center and the other 4 in the edges of the film) at a magnification of 500X. The chemical composition of the deposited coatings was found homogeneous throughout the film. EDS Ca/P values compiled in Table 1 correspond to mean values and their respective standard deviations. Moreover, the average thickness of CaP coatings was determined on cross-sectioned silicon wafer.

Powder X-ray diffraction (XRD) was performed using a PANalytical X'Pert PRO MPD diffractometer, employing Cu $K\alpha_1$ radiation with λ = 1.54056 Å. The data were collected in the Bragg–Brentano geometry in 2Θ range from 10° to 55°, with a 0.033° step width and ~10 s/step time. The obtained crystalline phases were identified by comparison with the powder diffraction file (PDF) from the International Centre for Diffraction Data (ICDD). A refinement of lattice parameters was performed by profile matching calculated using the Bruker DIFFRAC.EVA® *v.4.2* software. The crystallite size was calculated by the Scherrer equation [44,45] using the *002*, *210*, *300*, and *202* diffraction peaks. A nanocrystalline HAP XRD pattern was simulated (Mercury 3.10.3) based on published cell parameters PDF# 01-074-0565. This simulated XRD pattern was employed as a pure HAP reference signal for comparative purposes.

Infrared and Raman spectra were obtained to characterize the molecular structure of the deposited coatings on Ti6Al4V substrates. Fourier transform infrared spectroscopy (FTIR) in reflection was carried out from 4000 to 400 cm^{-1} with a resolution of 2 cm^{-1} and 64 scans (ATR mode, Thermo Scientific Nicolet iS50). Raman characterizations were performed using a Renishaw InVia Raman spectrometer equipped with dielectric filters to remove the Rayleigh line. Raman photons were collected with a cooled CCD detector. In all cases, the 514.5 nm line (green light) from an Argon ion laser was used as the excitation source. It was focused on the sample through an objective (G = 50). The power reaching the sample was 3-4 mW.

A commercial HAP powder (SAI, MedicalGroup) was used to acquire the reference FTIR and Raman spectrum.

The Ca/P molar ratio of as-deposited coatings was accurately determined by inductively coupled plasma-optical emission spectrometry (ICP–AES, Varan 720ES) against standard solutions (P(V), Chem-Lab, 1000g. L^{-1} (CL01.0641.0100), Ca(II), Roth, 1000g. L^{-1} (2407.1)) [46,47]. Working solutions were prepared from the dissolution of the films in 0.5 mL ultrapure nitric acid (Sigma-Aldrich, 65 %,), left to stand overnight at 80 °C and then, Milli-Q® water was added to reach 10 mL in volume and a concentration of ~5 ppm Ca(II). Ca 373 nm, P 213 nm wavelengths were chosen to calculate the Ca/P ratio in as-deposited coatings. Repeatability and reproducibility were evaluated by making 3 injections of the same solution and 4 different runs of all the solutions (calibration curve and coating solutions).

2.4 Heat treatments

The crystallization behavior of CaP coatings and their reactivity with Ti6Al4V substrates were investigated using XRD and Raman spectroscopy. Some as-deposited coatings were post-annealed according to two different heat-treatments in air, either a conventional one in a furnace up to 700 °C and 800 °C at a heating rate of 15 °C min^{-1} for 60 min, or a fast-radiant heating, under an infrared lamp up to 700 °C at a heating rate of 300 °C min^{-1} for 15 min.

3. Results

3.1. The influence of precursor content on the composition of as-deposited films

The effect of the molar ratio of the precursors was studied by keeping the Ca(II) concentration constant at 15 mM and varying the TEP concentration from 9 mM to 75 mM in pure ethanol. The measured Ca/P molar ratios of the as-deposited coatings, determined using EDS and ICP/AES analyses, are presented in Fig. 1. Irrespective of the analytical technique, one can observe two domains in the evolution of the observed Ca/P ratios. Below a nominal Ca/P molar ratio of 0.8, the observed ratio remains constant and close to the stoichiometric ratio of 1.67 (for pure, stoichiometric HAP). Above this critical value, the observed Ca/P ratio increases linearly with the nominal one, to reach ~3 for a nominal ratio of 1.67. In all cases, the EDS values are always larger than the ones deduced from ICP measurements. For instance, on the plateau obtained at a low nominal Ca/P ratio (≤ 0.8), the observed Ca/P ratio is ~1.9 by EDS and ~1.6 by ICP (Fig. 1). This difference could be assigned to a systematic error caused by the expulsion of P atoms under the electron beam. The following obtained EDS values with a Ca/P ratio of ~1.9 will be assigned to a pure hydroxyapatite coating.

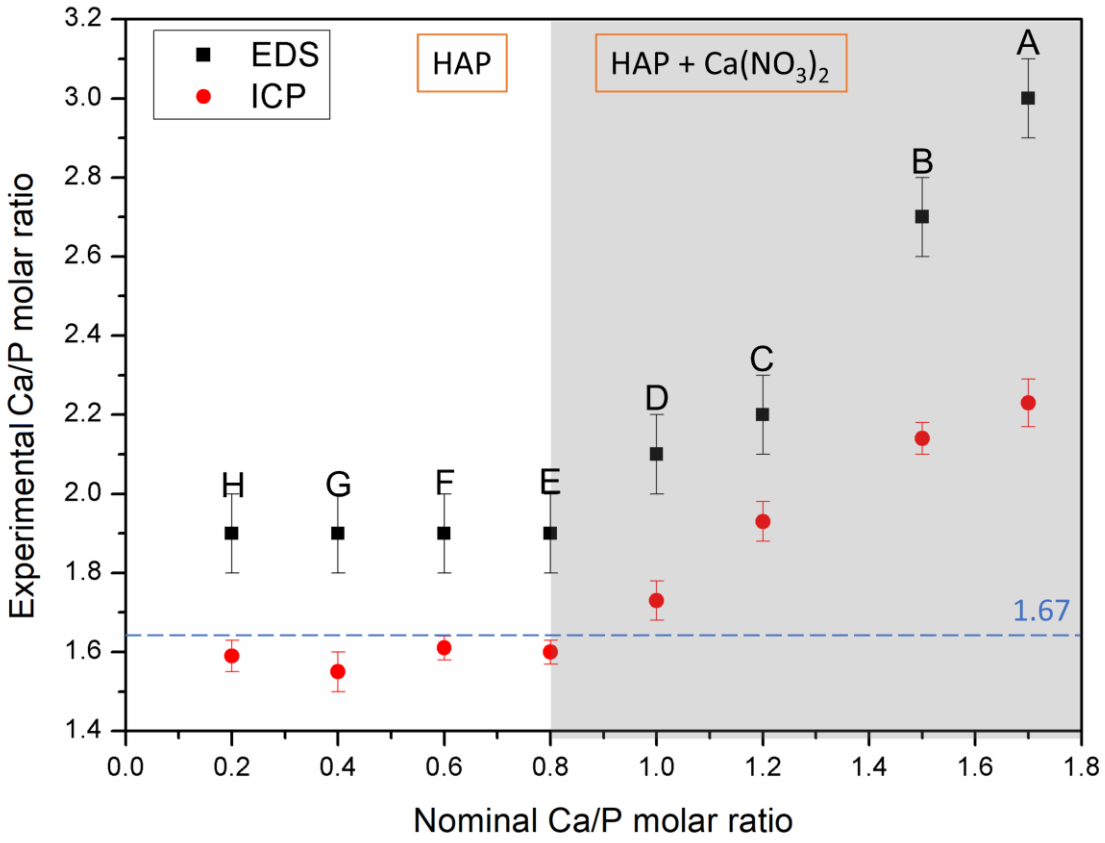

Fig. 1. The experimental Ca/P molar ratio of as-deposited coatings measured by EDS and ICP versus the nominal ones. Solutions A and E will be referred to as SA and SE in the following.

The X-ray diffraction patterns of as-deposited CaP films are shown in Fig. 2**I**. The crystalline hydroxyapatite (HAP) phase was identified in all samples and indexed to a hexagonal unit cell with a $P6_3/m$ space group (#176) according to PDF# 01-074-0565. A refinement of lattice parameters performed only on the pure crystalline HAP phase obtained at 350 °C (sample E), as a first approach, led to a = 9.430 Å, and c = 6.882 Å. The Ti6Al4V substrate (Hexagonal, $P6_3/mmc$ space group, #194, PDF# 04-002-8708) is also detected. Furthermore, one can observe a slight broadening of HAP peaks

coherent with a decrease in the crystallite size (Figure 2**I**) when increasing the P(V) content in the precursor solution (for lower Ca/P ratios).

In the Raman spectra (Fig. 2**II**), for nominal values of Ca/P ratio larger than 0.8 (SA; Ca/P = 1.67), in addition to the spectral signature of HAP, bands are observed at 750 cm^{-1} and in the 1000 - 1100 cm^{-1} range, typical of NO_3^- group coming from $Ca(NO_3)_2$. A mixture of HAP with $Ca(NO_3)_2$ is obtained, as indicated by a grey area in Fig. 1. Since the calcium nitrate phase is not detected by XRD, one can assume that this second phase is amorphous. When a lower nominal Ca/P ratio (SE; Ca/P = 0.8) is used, only the Raman bands assigned to hydroxyapatite are observed (400 - 490, 570 - 625 and 1020 - 1095 cm^{-1}, originated from the ν_2 (doubly degenerated), ν_4 (triply degenerated) and ν_3 PO_4^{3-}-tetrahedron modes, respectively, and the single strongest peak at 962 cm^{-1} assigned to the non-degenerated ν_1 PO_4^{3-} mode of HAP [48]).

Thus, the phases formed depends strongly on the content of the precursors in the initial solution. In the following, the term "optimized" precursor solution will refer to a Ca/P ratio below or equal to 0.8 (and "non-optimized" for a ratio above 0.8). Using ethanol as solvent, the optimized phase gives rise to the pure HAP phase whereas the "non-optimized phase" results in a HAP + $Ca(NO_3)_2$ mixture.

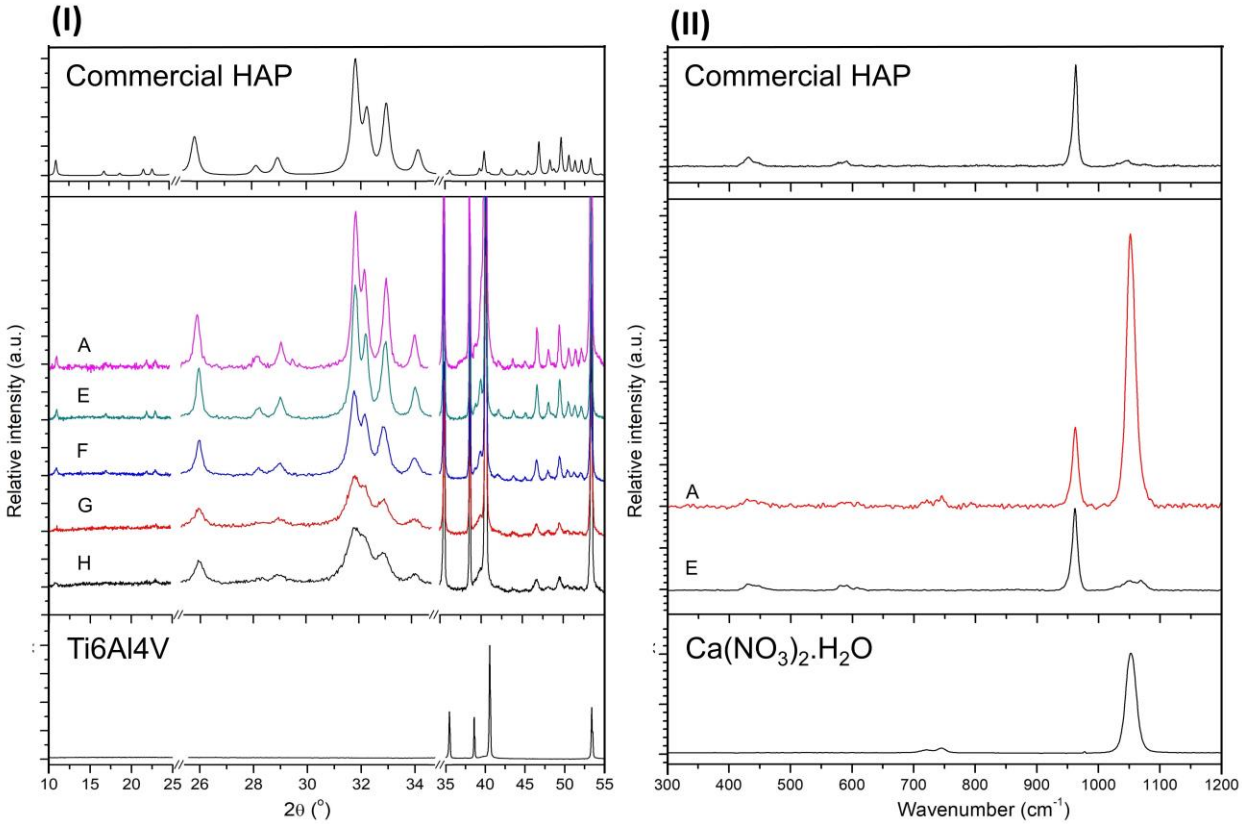

Fig. 2. (I) XRD patterns of as-deposited coatings (A; E to H) prepared at 350 °C using ethanolic solution with different nominal Ca/P molar ratios at a constant Ca(NO3)2 concentration of 15 mM and different concentrations of TEP: (SA) 9 mM; Ca/P = 1.67; (SE) 18.75 mM; Ca/P = 0.8; (SF) 25 mM; Ca/P = 0.6; (SG) 37.5 mM; Ca/P = 0.4; (SH) 75 mM; Ca/P = 0.2. For the sake of clarity, the XRD pattern of the film obtained with SA represents the series from A to D. (II) Raman spectra of films obtained with SA, representative of the series from A to D, and SE representative of the series from E to H.

3.2. Morphology of as-deposited films

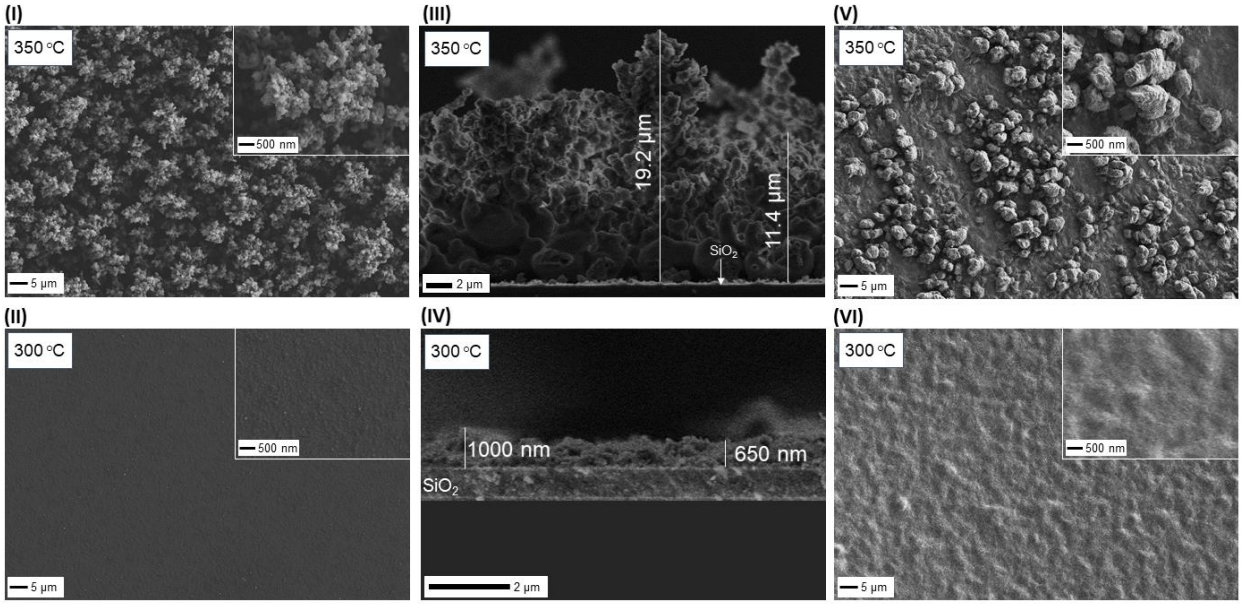

Fig. 3. SEM observations of as-deposited films, for a needle-to-substrate distance of 30 mm, a flow rate of 1.5 ml h-1, and a deposition time of 1.5 h. for (i) the SE optimized precursor solution (15 mM Ca(NO3)2, and 18.75 mM TEP in pure ethanol, Ca/P = 0.8), at (I) 350 °C, (II) 300 °C; SEM cross-section on top of Si wafer at (III) 350 °C, (IV) 300 °C; (ii). a solution containing 15 mM Ca(NO3)2, and 9 mM TEP in pure BC (Ca/P = 1.67) at (V) 350 °C, and (VI) 300 °C. Insets are given for a larger magnification.

Fig. 3**I** and Fig. 3**II** show SEM observations of CaP coatings deposited with the SE optimized solution (Ca/P molar ratio of 0.8) using ethanol as solvent at 350 and 300 °C, respectively. At 350 °C, a highly porous, 3D coral-like morphology of ~15 µm thick (Fig. 3**III**) is observed. From previous structural characterizations (Fig. 2**I**), only the HAP phase is obtained at 350 °C. The average particle size is estimated to be around 260 ± 70 nm (ImageJ®) from image analysis. This precursor solution based on ethanol has a low boiling point and, consequently, at 350 °C leads to a high evaporation rate of the solvent during the flight time. At a lower temperature of 300 °C, denser films (Fig. 3**II**), ~800 nm thick (Fig. 3**IV**), can be observed. The boiling point of the solvents and the substrate temperatures are parameters that strongly affect the size of the droplets impacting the heated substrate and, therefore, the microstructure of the coating. As an example, Fig. 3**V** and Fig. 3**VI** show surface observations of CaP coatings deposited using BC as solvent (Ca/P molar ratio of 1.67) at 350 and 300 °C, respectively. Working with solvents of high boiling points, such as BC, denser-like-film are obtained even for the film deposited at 350 °C (Fig. 3**V**).

3.3. Influence of the solvents on the experimental Ca/P molar ratio of as-deposited films

3.3.1. Influence of addition of water in the precursor solution

Five different compositions of the precursor solutions (highlighted in grey in Table 1) have been investigated to explore the influence of addition of water on the chemical composition of the ESD coatings. Different mixtures of solvents such as EtOH 100%; EtOH: H_2O (19:1); EtOH: H_2O (1:1); EtOH: H_2O (19:1) + 2 mM NH_3; EtOH: H_2O (19:1) + 2 mM HNO_3 were prepared to take advantage of their different physicochemical properties, such as boiling point, surface tension, and electrical conductivity (Table 1). In all cases, $Ca(NO_3)_2$ and TEP concentrations were fixed to 15 mM and 9 mM, respectively, to keep a nominal Ca/P ratio of 1.67. Other deposition parameters remained constant, except for the voltage, which was adjusted to get a stable Taylor-cone regime [42,43]. Moreover, the depositions were performed at two different temperatures, i.e. 300 and 350 °C.

For these solutions, the droplet sizes were estimated according to Equation 1 and found in the range of 2.2 to 3.5 µm (Table 1). From EDS data, the Ca/P ratio strongly decreases when the water content in the solution increases. Indeed, when the solvent changes from pure EtOH to EtOH: H_2O (1:1), the observed Ca/P molar ratio decreases from 6.4 to 2.9 when the substrate temperature is 300 °C and from 3.0 to 2.5 at 350 °C. Since the Ca/P ratio is found to be similar in the coatings deposited using either a solution with 2 mM of NH_3 or HNO_3, the effect of acidic or alkaline catalysis is found negligible in these conditions. Besides, solutions with less water content, i.e. EtOH: H_2O (19:1), were subjected to an aging treatment in similar acidic and alkaline conditions for 24 h at 60 °C. The Ca/P ratios were found to be similar to the values obtained from solutions without aging.

3.3.2. Influence of the boiling point of the solvents

Several solvents with different boiling points were used in the precursor solutions to deposit CaP coatings at two different temperatures, 300 and 350 °C. The values of estimated boiling points of the precursor solutions are listed in Table 1 in ascending order. Ethanol (CH_3-CH_2OH, EtOH herein) and butyl carbitol (diethylene glycol monobutyl ether, $C_4H_9(OCH_2CH_2)_2OH$, BC herein) were chosen for their low and high boiling points, 78 °C and 231 °C, respectively. Methanol (CH_3-OH, MetOH herein) and 1-butanol (CH_3-$(CH_2)_2$-CH_2OH, ButOH herein) were selected because the solvent-precursor interactions are similar to those with EtOH and they offer lower or intermediate boiling points. Ethylene glycol (CH_2OH-CH_2OH, EG herein) was interesting as a solvent of high boiling point, 198 °C, that could interact better with TEP than with BC during flight time due to its -OH groups. Milli-Q® H_2O was added to some of the solutions to vary their boiling points.

As reported in Table 1Table 1, the droplet sizes at the tip of the needle for these precursor solutions are estimated in the range of 2.2 to 5.6 µm from Equation 1. EDS results show that the measured Ca/P molar ratios are strongly dependent on the chosen solvent. A tendency to obtain smaller Ca/P ratios is more visible at a substrate temperature of 350 °C than at 300 °C, as reported above. One can also observe that the smaller Ca/P molar ratios are related to the smaller droplet sizes at all temperatures. Ca/P molar ratio of the deposited coating can only be quantified when a primary-alcohol solution is used as a solvent, such as MetOH, EtOH, and ButOH. In all other cases, for solvents characterized by boiling points higher than 118 °C, the phosphorus content is below the detection threshold (referred to as D.T., Table 1), whatever is the substrate temperature.

FTIR spectra of coatings obtained at a substrate temperature of 350 °C are given in Fig. 4. The coatings were prepared from precursor solutions based on EtOH: H_2O (19:1), EtOH; EtOH: EG: H_2O (18:1:1), EtOH: EG (19:1), EG and, BC, keeping constant the nominal composition to 15 mM $Ca(NO_3)_2$ and 9 mM TEP, thus Ca/P ratio of 1.67 (Table 1). For solutions based on solvents with a high boiling point such as EG and BC, $Ca(NO_3)_2$ signals (NO_3^- vibrational modes – $\nu_3 = 1360$ cm^{-1} and $\nu_2 = 813$ cm^{-1} – plus H_2O absorption bands) and peaks of $CaCO_3$ ($\nu_3 = 1430$ cm^{-1}; $\nu_2 = 876$ cm^{-1} and $\nu_4 = 712$ cm^{-1}), due to $Ca(NO_3)_2$ decompositions, are observed on the FTIR spectra. The additional spectral signature of HAP, characterized by PO_4^{3-} bands (highlighted by a frame in Fig. 4), is only observed when solvents with a low boiling point are used, EtOH and EtOH: H_2O (19:1), as confirmed by EDS data.

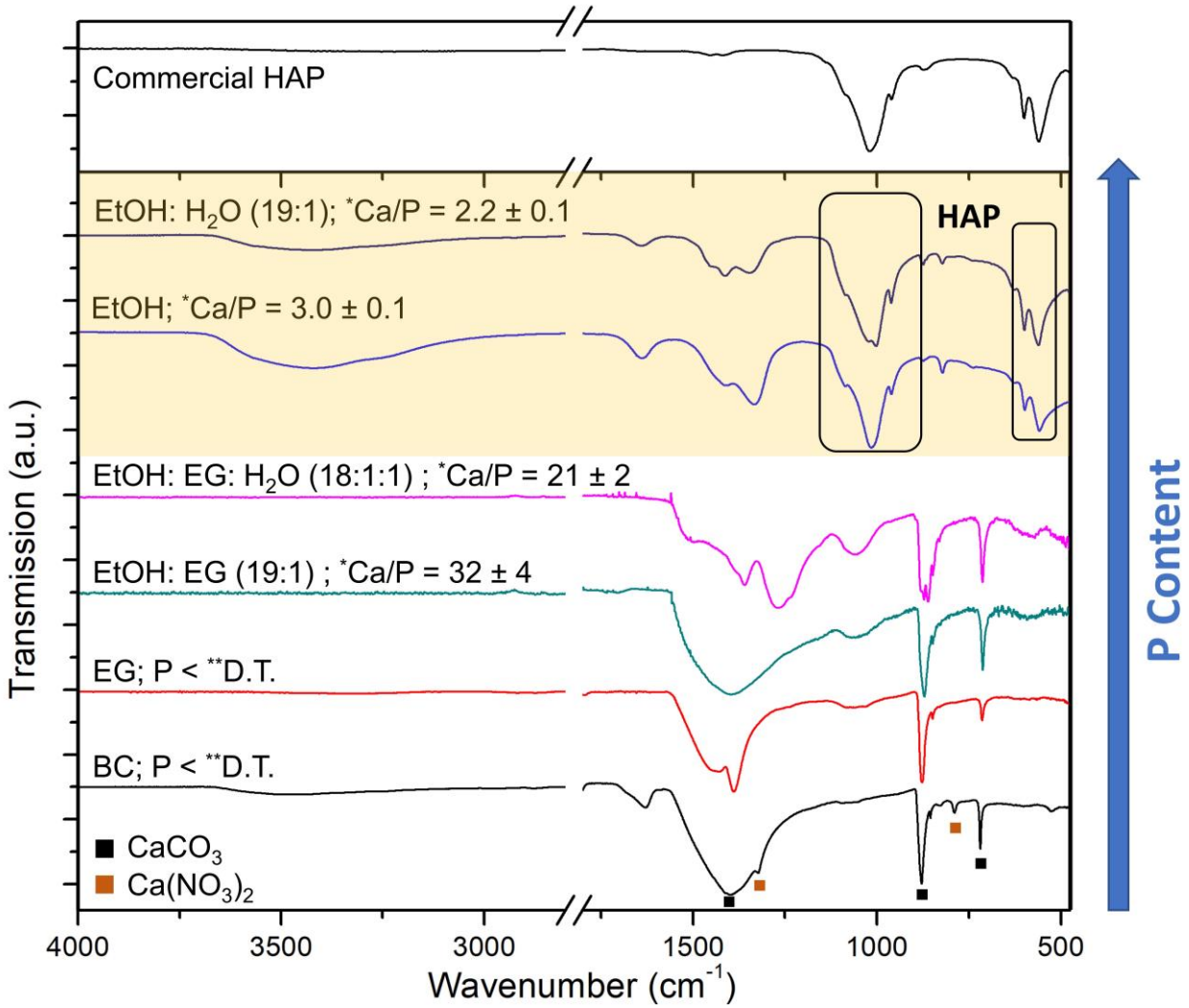

*Fig. 4. FTIR spectra of as-deposited coatings at 350 °C for different solvents using a needle-to-substrate distance of 30 mm, a flow rate of 1.5 ml h^{-1} a deposition time of 1.5 h. The nominal composition is 15 mM $Ca(NO_3)_2$, and 9 mM TEP (thus Ca/P = 1.67) for all solutions. *Ca/P ratios are measured by EDS. **D.T. = detection threshold.*

The formation of single-phase HAP coatings is dependent on the boiling point of the solvent and the water content of the solution. To examine the competition of hydrolysis over the evaporation of phosphorus precursor, a small amount of H_2O and/or ethylene glycol was added to an ethanolic solution. As seen in Table 1Table 1, at 350 °C, even the addition of a small quantity, 5 %vol./vol., of a solvent with a high boiling point, such as EG in EtOH, leads to a large Ca/P molar ratio of 32. If a small amount of H_2O is added to the EG/EtOH mixture, the ratio is slightly decreased to 21. For ethanolic solution, a small amount of ethylene glycol favors P(V) precursor evaporation, while the addition of water helps to retain it in the droplets that impact the substrate. Indeed, FTIR analysis (Fig. 4) indirectly confirmed the tendency towards evaporation of TEP when ethylene glycol is added to the solution.

3.4. Influence of the substrate temperature on the experimental Ca/P molar ratio and structure of as-deposited coatings

Structural properties of as-deposited coatings prepared for two different nominal Ca/P molar ratios of 1.67 and 0.8 (solutions SA and SE, respectively) were characterized by FTIR and XRD (Fig. 5). The substrate temperature was varied from 300 °C to 400 °C by steps of 25 °C. The final Ca/P ratio was determined by EDS analysis.

At 300 °C, for both solutions, the measured Ca/P molar ratio is around 6. The FTIR spectra of as-deposited coatings (Fig. 5**II** and **IV**) show weak PO_4^{3-} signals in contrast to strong NO_3^- and water absorption bands. The small phosphate signature is probably related to the predominant evaporation of TEP (boiling point of 215 °C [49]) during the ESD process. The other bands are associated with unreacted Ca(II) nitrate precursor, as previously reported in §3.3.2., (NO_3^- vibrational modes - ν_3 = 1360 cm^{-1} and ν_2 = 813 cm^{-1}), peaks of $CaCO_3$ (ν_3 = 1430 cm^{-1}; ν_2 = 876 cm^{-1} and ν_4 = 712 cm^{-1}) due to partial decomposition of $Ca(NO_3)_2$ during the deposition process, and H_2O absorption bands coming from the inherent hygroscopic behavior of $Ca(NO_3)_2$). XRD shows only the diffraction peaks of the Ti6Al4V substrate, signifying that the coatings are amorphous (data at 300 °C are not shown here).

When the temperature is increased from 325 °C to 400 °C, the Ca/P ratio converges to constant values of ~3 for SA and ~1.9 for SE. The value of ~1.9 for SE, measured by EDS, does correspond to a pure HAP coating as shown in §3.1. It seems that a larger quantity of P(V) precursor, present in SE, is required to favor the reactivity over the evaporation process of TEP, leading to a Ca/P molar ratio closer to the one of HAP. In all cases, XRD shows that HAP is the only crystalline CaP phase. FTIR spectra show characteristic bands of the PO_4^{3-} groups of HAP for the coating obtained from both solutions. Indeed, the bands at 1020-1120 cm^{-1} are assigned to the triply degenerate asymmetric stretching mode, ν_3, of the P-O bond. P-O symmetric stretching mode, ν_1, is detected at 960 cm^{-1} while the bands at 563, 571, and 599 cm^{-1} are assigned to the triply degenerated bending mode, ν_4, of the P-O bond. Finally, hydroxyl group signals are located at 630 cm^{-1} for the vibrational mode and 3568 cm^{-1} for the stretching mode [50]. One can observe additional FTIR bands in coatings obtained with SA (with a lower TEP content than in SE) related to unreacted Ca(II) precursor and H_2O absorption bands, as what was observed at 300 °C. This is consistent with the formation of a mixture of HAP and $Ca(NO_3)_2$ as reported in §3.1.

Thus, using the optimized solution SE and substrate temperature above 325 °C, one can deposit well-crystalline, single-phase, slightly carbonated hydroxyapatite coatings. When the substrate temperature is increased from 325 °C to 400 °C, XRD patterns of as-deposited coatings show narrower peaks revealing an increase of the average crystallite size of HAP from 23 ± 3 nm to 39 ± 3 nm, respectively, for coatings obtained with solution SE (Table S1). This is expected since crystal growth is driven by a diffusion phenomenon.

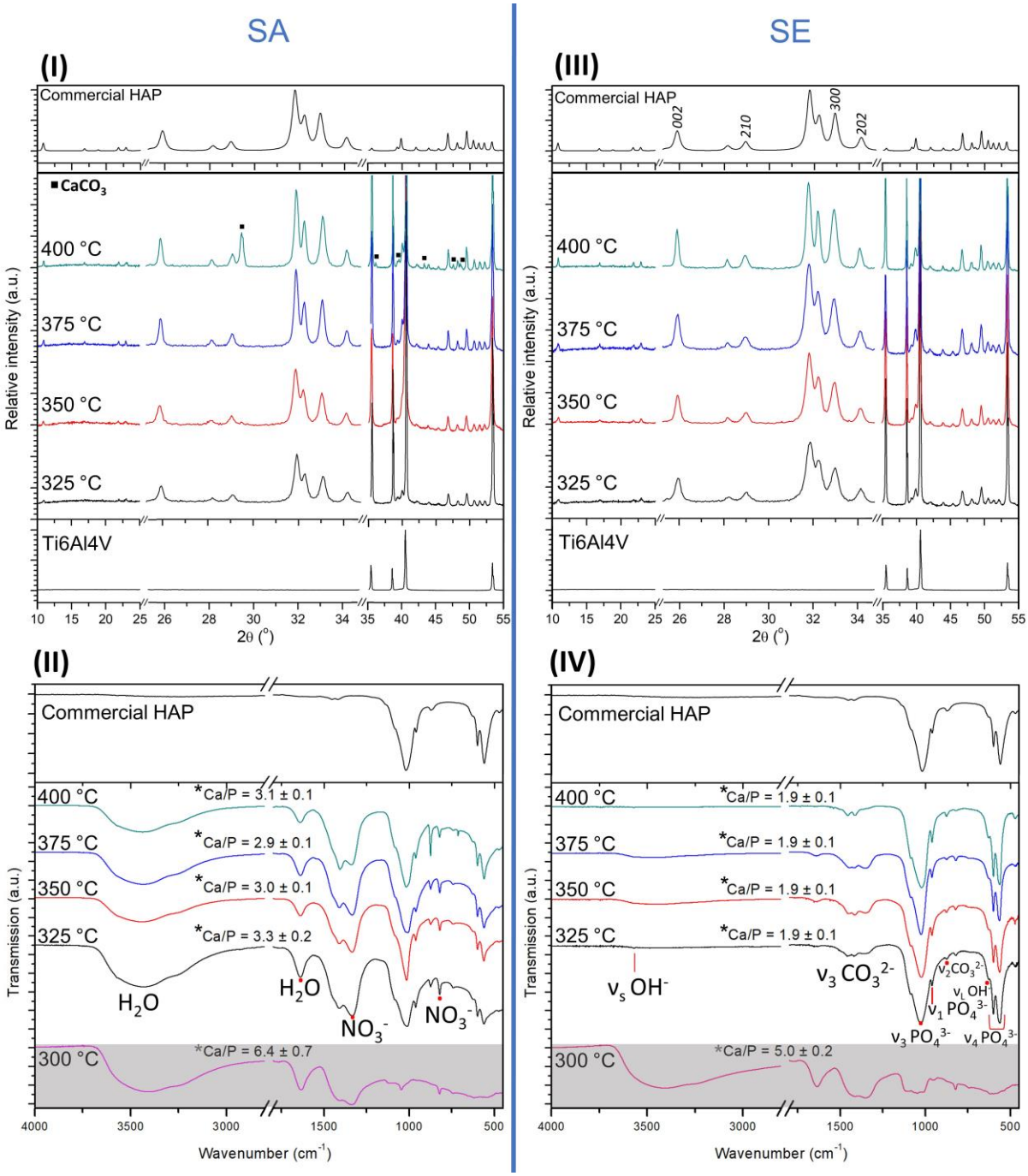

*Fig. 5. XRD patterns **(I, III)** and FTIR spectra **(II, IV)** of CaP coatings prepared by ESD, using two solutions: SA (nominal Ca/P = 1.67, 15 mM $Ca(NO_3)_2$; 9 mM TEP in EtOH), and SE (nominal Ca/P = 0.8, 15 mM $Ca(NO_3)_2$; 18.75 mM TEP in EtOH) with a needle-to-substrate distance of 30 mm, a flow rate of 1.5 ml h^{-1} and a deposition time of 1.5 h at different substrate temperatures from 300 °C to 400 °C. The hkl indices assigned to the commercial HAP diffractogram are the ones used to calculate the crystallite size from Scherrer formula [44,45]. (*) Ca/P ratios are measured by EDS.*

3.5. Influence of post-annealing on the structure of CaP coatings

The influence of the post-deposition annealing treatments described in §2.4 was evaluated on 2 types of coatings, obtained from solutions SE and SA with a 350 °C substrate temperature. The Ca/P ratios measured by EDS were found to be similar to those of the as-deposited coatings, whatever is the heat-treatment. In the case of a conventional heat-treatment, strong oxidation of the substrate appears at

temperatures above 800 °C, with the formation of rutile and traces of anatase, as shown by Raman spectroscopy in Fig. 6**I**. When the conventional annealing is performed at 700 °C, only CaP signals are observed in the Raman spectra.

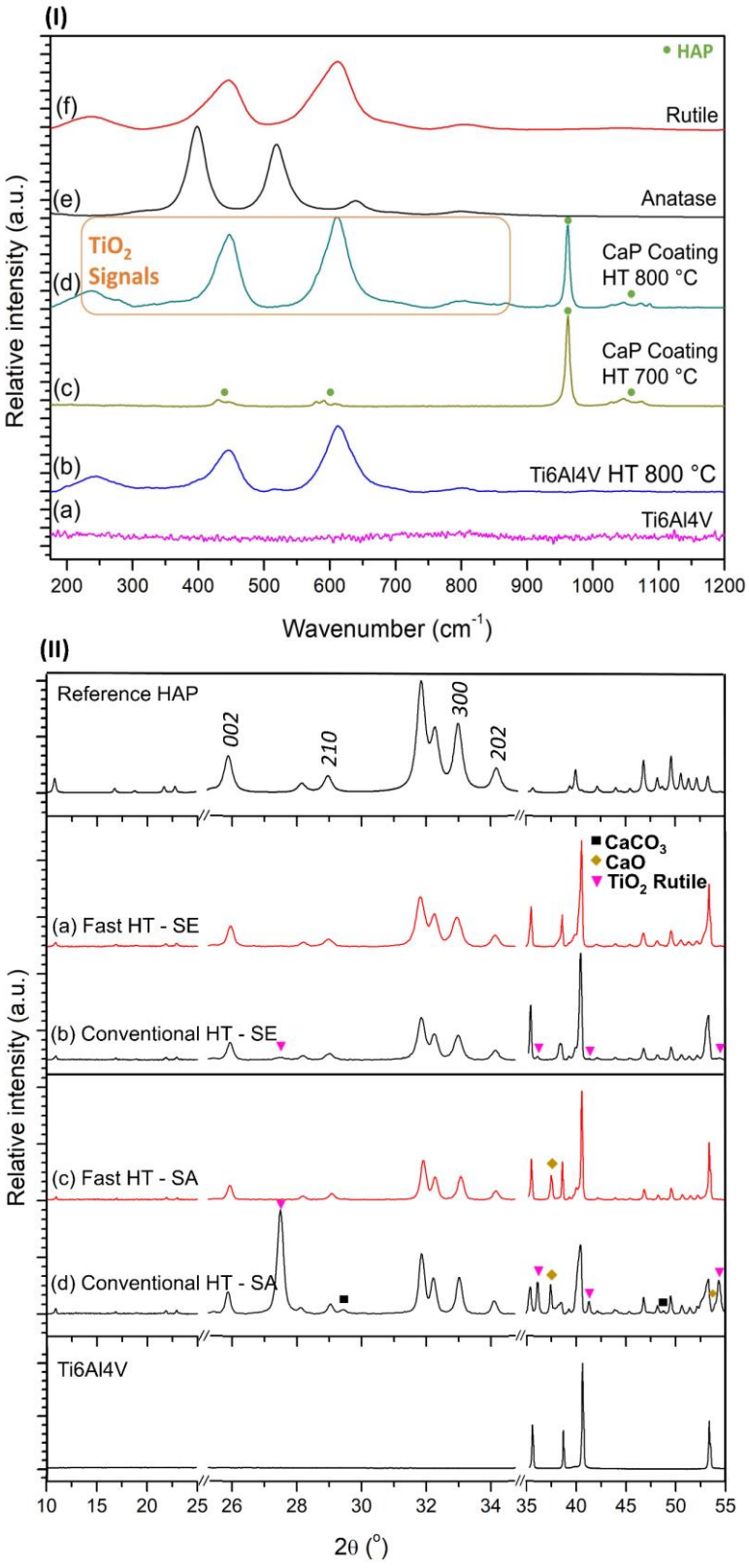

*Fig. 6. **(I)** Raman spectra of (a) pristine Ti6Al4V substrate; (b) Ti6Al4V substrate after conventional heat-treatment (HT) at 800 °C; CaP coatings obtained with SE solution after conventional HT at (c) 700 °C; (d) 800 °C; (e) TiO_2, anatase phase; (f) TiO_2 rutile phase. **(II)** XRD patterns of films after HT up to 700 °C (a) under IR lamp and (b) in conventional HT obtained from SE, (c) under IR lamp and (d) in conventional heating obtained from SA. The hkl indices assigned to the commercial HAP diffractogram are the ones used to calculate the crystallite size from Scherrer formula [44,45]. The conventional HTs are carried out in a furnace at a heating rate of 15 °C min^{-1} for 60 min. Fast ones are performed under an infrared lamp at a heating rate of 300 °C min^{-1} for 15 min. Depositions were performed at a substrate temperature of 350 °C, a needle-to-substrate distance of 30 mm, a flow rate of 1.5 ml h^{-1}, and a deposition time of 1.5 h.*

XRD patterns of films obtained from SA and SE and heat-treated using both conventional and fast heat-treatments are shown in Fig. 6**II**. In all diffractograms, the crystalline HAP phase can be identified according to PDF# 01-074-0565.

When using a conventional heat-treatment, additional TiO_2 (rutile) peaks are observed (Fig. 6**II**(d) and Fig. 6**II**(b)). This rutile phase is coming from the oxidation of the Ti-substrate due to a longer heating exposure in the air during conventional heat-treatment. When using the non-optimized solution SA (Fig. 6**II**(d)), peaks assigned to $CaCO_3$ (PDF# 01-086-2343) and CaO (PDF# 01-082-1691) secondary phases are also detected, in good agreement with our previous results reported above.

When using a fast heat treatment, resulting in a shorter heating exposure in air, no traces of TiO_2 can be detected by XRD even if titanium oxidizes easily. A thin oxide layer could be present but is not detectable because it is in the XRD detection threshold or because it remains amorphous. Coatings obtained with non-optimized solution SA show no presence of $CaCO_3$, while CaO is still present, certainly resulting from the non-optimized composition of the SA precursor solution.

As a result, a fast heating rate is favorable to prevent Ti oxidation and leads, in the case of a coating deposited with the optimized solution SE, to a single HAP phase (Fig. 6**II**(a)). In the latter case, the average crystallite size of the HAP phase increases from 30 ± 4 nm in as-deposited films to 50 nm ± 3 after the heat treatment, whatever is the heating rate. No trace of chemical reactivity was detected between the Ti6Al4V substrate and the HAP coating (within the detection limits of Raman spectroscopy and XRD, Fig. 6). SEM observations of these coatings obtained in optimal conditions are reported in Fig. S1. No microstructural modification can be observed after heat-treatment.

4. Discussion

In this study, particular attention has been given to the deposition of pure electro-sprayed HAP films with an accurate determination of their Ca/P atomic ratios and phase purity. The samples were subjected to in-depth structural, microstructural, and compositional analyses using XRD, Raman spectroscopy, FTIR, SEM-EDS, and ICP-AES.

4.1. Control of the Ca/P ratio – Deposition of single-phase HAP

Briefly, ESD is a coating process based on the generation of micron-sized electrically-charged droplets created due to a difference of potential between a nozzle and a grounded and heated substrate [51]. After complete or partial droplet evaporation during the flight from the nozzle to the substrate, a thin inorganic layer is produced at the surface of the substrate. Generally, the precursor solution contains only inorganic reagents [31,38]. Hence, the phenomenon of evaporation is limited to the solvent. However, in this work, the scenario becomes more complex, since an organic P(V) precursor has been used, TEP, and three main effects need to be considered to obtain single-phase HAP coatings: the evaporation of the solvent, the evaporation of the phosphorus precursor, and its hydrolysis.
Thus, the main parameters that enable the control of the final Ca/P molar ratio are the following: the H_2O content, the boiling point of the solvents, the substrate temperature, and the nominal Ca/P molar ratio in the precursor solution.

4.1.1. Influence of addition of water in the precursor solution

$Ca(NO_3)_2.4H_2O$, is observed to completely dissociate in the conditions used here, bringing enough crystallization H_2O molecules to fully hydrolyse TEP and produce HAP quantitatively. One mole of

pure HAP requires 10 moles of water (9 moles for the hydrolysis of 3 moles of TEP and one mole for the remnant -OH). Thus, there is a 100 % excess for the stoichiometric reaction, irrespective of the solvent. Assuming that Ca(II) ions remain in solution and are quantitatively deposited onto the substrate, the measured Ca/P ratio, systematically lower than the nominal one, offers straight evidence of the TEP loss percentage.

The addition of water to a low boiling point precursor solution, such as ethanol, was found to increase phosphorus content in the ESD coating (Table 1). Indeed, during the flight time, the solvent evaporates and as a consequence, the reagent concentration for the hydrolysis process is increased. Besides, neither the addition of acid or base nor the aging of the precursor solution, for 24 h at 60 °C, contributes to the increase of P content in the coating compared to the use of the non-aged solutions. Partial hydrolysis of TEP during aging for 24 h is negligible. Consequently, the final reactivity of P(V) precursor is not affected under spraying. It has been reported that phosphoric acid triesters are readily hydrolyzed in acidic and alkaline solution to the corresponding diesters, but subsequent hydrolysis stages are relatively slow [52]. If the substrate temperature is increased from 300 °C to 350 °C, the Ca/P molar ratio approaches the nominal composition, certainly because the chemical decomposition of the triethyl phosphate is more pronounced when the deposition is carried out above the thermal barrier of 325 °C, as discussed in §4.1.3. At 350 °C, TEP loss in an ethanol solution can be significantly reduced by increasing the initial water content (from 5 to 50 % vol./vol.). However, TEP evaporation still takes place even in the presence of a large excess of water.

4.1.2. Influence of the boiling point of the solvents - Solvent evaporation

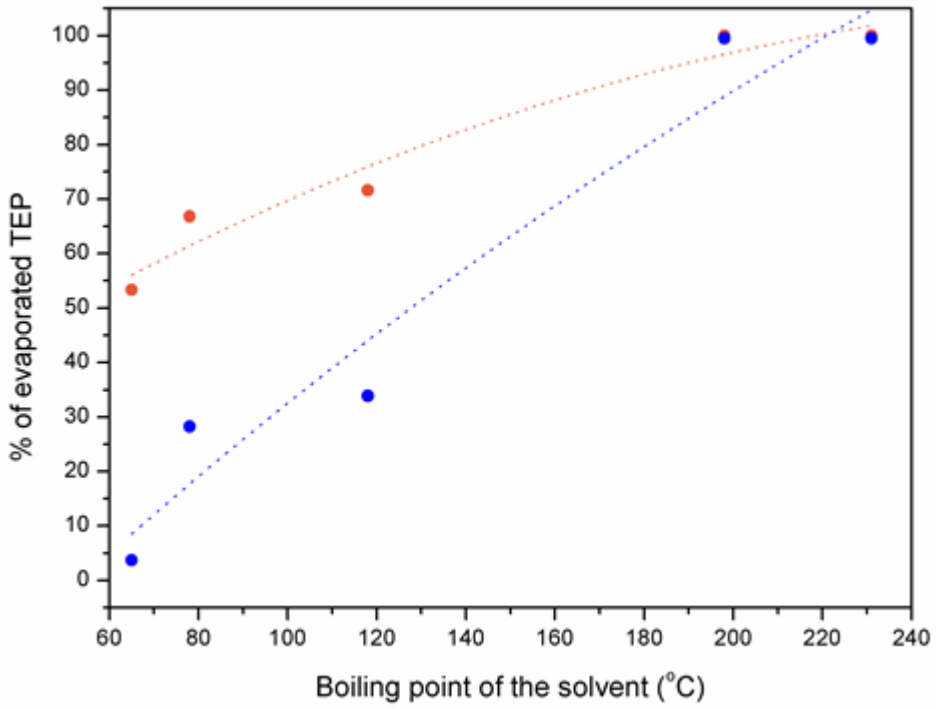

Fig. 7. Percentage of evaporated TEP as a function of the boiling point of the solvent for two different temperatures of deposition: 300 °C (orange dots) and 350 °C (blue dots) with the SA nominal composition (15 mM $Ca(NO_3)_2$, and 9 mM TEP, Ca/P = 1.67). A needle-to-substrate distance of 30 mm, a flow rate of 1.5 ml h^{-1}, and a deposition time of 1.5 h. were used for all ESD films. Dotted lines are a guide to the eyes.

The boiling point of the solvent in the precursor solution is an important parameter to control, which influences the quality of the aerosol and the droplet size impacting the substrate. The solvent evaporation during the ESD process can be regulated by a careful choice of the boiling point of the solvent mixture, the temperature of the substrate, the needle-substrate distance, and the flow-rate of the precursor solution, all of which can alter the flight time of droplets. In summary, it is the size of the droplets when impacting the hot substrate and the combined effects of the spreading and drying speeds that determine the morphology of the layer (Fig. 3). Beyond the precise design of the coating microstructure, the chemical composition of the films must be perfectly controlled. From EDS results (Table 1), one can observe that the final Ca/P ratio increases with the boiling point of the solvent, probably due to large evaporation of P precursor during the deposition process (Fig. 7). The content of evaporated TEP is even more pronounced at a substrate temperature of 300 °C than at 350 °C. If a solvent of high boiling point, such as EG (b.p. = 198 °C [40]) or BC (b.p. = 231 °C [40]) is used, water molecules from Ca(II) precursor and TEP loss are dramatically favored. The quantitative loss of TEP by evaporation prevails over decomposition, irrespective of the substrate temperature. Indeed, $Ca(NO_3)_2$ and $CaCO_3$ FTIR signals are observed in as-deposited coatings under these circumstances. The origin of partial calcium nitrate decomposition into calcium carbonate can be explained by the chemical reaction between the remaining organic solvent and the calcium source. Additionally, if an excess of water is added to the solution, i.e. EG: H_2O (1:1) or BC: H_2O (1:1), the presence of a high boiling point solvent governs the overall behavior. H_2O and TEP are entirely lost during the process as in the aforementioned situation and the addition of extra water cannot compensate for the effect of a high boiling point solvent. Although in this work it is not possible to disentangle completely the hydrolysis and evaporation effects, it is nevertheless easy to assess their over-all effect. According to the Ca/P ratio observed in the coatings, the evaporation effect seems to dominate over the hydrolysis of the P precursor on the deposition process.

Droplet sizes at the tip of the needle, estimated from Equation 1, increase (Table 1) with the boiling point of the solvent. In the case of solvents of a high boiling point, larger droplets are formed, with a smaller surface/volume ratio than in the case of the smaller ones. During the flight, these large droplets thus undergo slower solvent evaporation, maintaining a larger dilution of the precursors in the solvent. Consequently, the phosphorus precursor, being more diluted, is subject to greater evaporation during the flight and/or when impacting the heated Ti6Al4V substrate. Likewise, the addition of a small quantity of solvent of a high boiling point, such as ethylene glycol to ethanol, exacerbates the evaporation of the P(V) precursor (Table 1). To obtain CaP coatings made of HAP (see Fig. 4), a solvent of low boiling point (EtOH and also MetOH) must be used to avoid the evaporation of the P(V) precursor and water during the deposition and to favor the TEP reactivity. Here for a non-optimized precursor solution, with a nominal Ca/P molar ratio of 1.67, the TEP concentration is only 9 mM, and maybe not enough to form HAP when solvents of a large boiling point are employed, even at 350 °C. So, it is of great importance to optimize the chemical composition of the precursors in the solution to produce a single-phase HAP coating.

Besides, when using a high boiling point solvent, the final Ca/P molar ratio could be controlled by strongly decreasing the nominal Ca/P molar ratio (or strongly increasing the nominal content of TEP precursor in the precursor solution). For instance, a Ca/P molar ratio of ~10 was measured by EDS using a solution of a nominal 0.4 Ca/P molar ratio in pure BC, while it was not possible to detect P(V) when this nominal Ca/P molar ratio was 1.67. In other words, evaporation of solvent and precursor are key processes in the deposition of a single-phase HAP coating using TEP as a P(V) precursor.

4.1.3. Influence of the substrate temperature on the chemical composition of CaP in as-deposited films

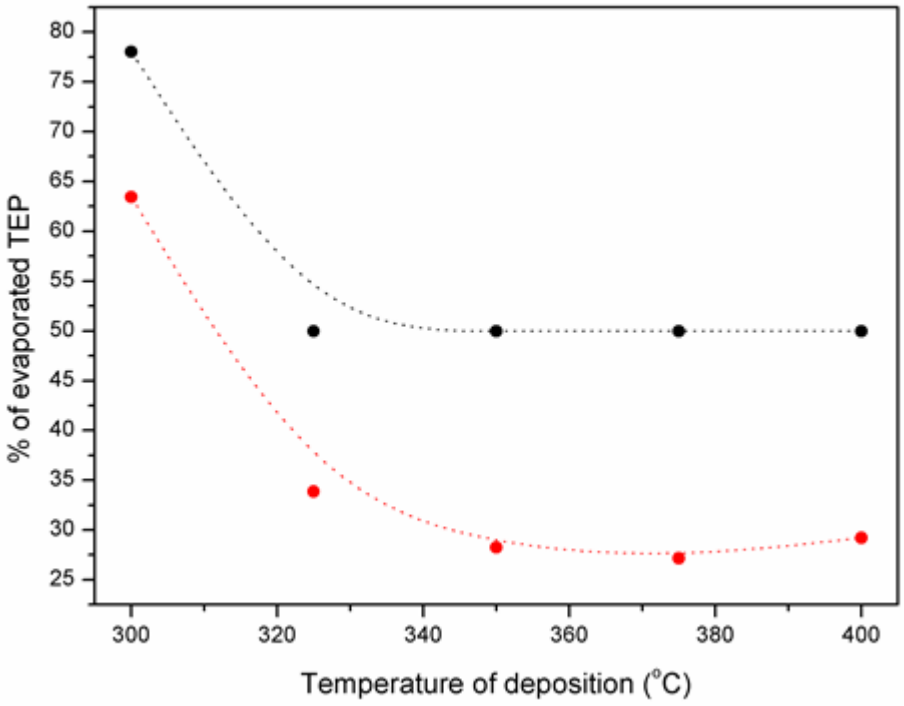

Fig. 8. Percentage of evaporated TEP as a function of the temperature of deposition for two ethanol solutions: SA (15 mM $Ca(NO_3)_2$ and 9 mM TEP, Ca/P = 1.67), (red dots), and SE (15 mM $Ca(NO_3)_2$ and 18.75 mM TEP, Ca/P = 0.8), (black dots). A needle-to-substrate distance of 30 mm, a flow rate of 1.5 ml h^{-1}, and a deposition time of 1.5 h. were used for all ESD films. Dotted lines are a guide to the eyes.

As it was mentioned before, that unlike inorganic precursors, the chemical composition of CaP films deposited using TEP is extremely dependent on the substrate temperature during the ESD deposition. Obtaining single-phase HAP coatings is governed by the decomposition of NO_3^- and the competition between reactivity and evaporation of TEP.

Fig. 8 shows the percentage of evaporated TEP versus the temperature of ESD deposition for two ethanolic solutions. At 300 °C, the complete chemical decomposition of TEP is not expected to occur. The large droplets, full of solvent, lose their water during the flight while the evaporation of TEP predominates. The TEP evaporation is a phenomenon that occurs mainly when the substrate temperature decreases, whatever is the composition of the precursor solution (SA or SE). These droplets, containing calcium nitrate and solvent in the majority, arrive in a liquid state and spread onto the heated substrate to produce dense films (Fig. 3). This scenario occurs especially for solvents of a high boiling point, but it also exists in a minor way for solvents of low boiling point. The FTIR spectra of three coatings, prepared from precursor solutions based on EtOH, EG and, BC at two different ESD temperatures, 300 and 350 °C, are given in Fig. S2. For solutions based on solvents of a high boiling point such as EG and BC, unreacted $Ca(NO_3)_2$ signals and peaks of $CaCO_3$ due to $Ca(NO_3)_2$ decompositions are observed on the FTIR spectra regardless of the substrate temperature. The additional spectral signature of HAP, characterized by PO_4^{3-} bands (highlighted by a frame in Fig. S2**II**), is only observed when the solvent of low boiling point (EtOH in this case) is used and for a substrate temperature of 350 °C.

In all cases, the final Ca/P molar ratio was found larger than the nominal value, showing that TEP always evaporates during the coating deposition. The TEP evaporation is a phenomenon typical of organic precursors that permanently take place under spraying of the ESD solution due to the gradient of temperature between the top of the needle at room temperature and the heated substrate, even while using a solvent of low boiling point (Fig. 8). After the evaporation of TEP precursor from solution SA (nominal Ca/P molar ratio of 1.67 and low phosphate content of 9 mM, in pure ethanol), an excess of Ca(II), that remains as $Ca(NO_3)_2$, is present in the coating at 300 °C (Fig. 5**II**). If the substrate deposition is 400 °C, $Ca(NO_3)_2$ excess partially decomposes into unstable CaO which easily transforms into $CaCO_3$ when in contact with air (Fig. 5**I**). To compensate for the large evaporation of TEP, a nominal Ca/P molar ratio of 0.8 is proposed in SE (larger phosphate content of 18.75 mM). In these conditions, enough TEP reacts to produce only a carbonated hydroxyapatite phase, $Ca_{10-x}(PO_4)_{6-x}(CO_3)_x(OH)_{2-x-2y}(CO_3)_y$ [53,54], above a substrate temperature of 325 °C. Indeed, FTIR analysis confirmed that carbonate anions were incorporated into the apatite structure during the precipitation process. This carbonate is coming mainly from the organic solvent [55] and/or from the TEP decomposition. However, one can note that the amount of C that the P(V) precursor could contribute to the formation of carbonate HAP is negligible towards the decomposition of the solvents. Carbonate absorption peaks at 870 (ν_2) and 1415 and 1453 cm^{-1} (ν_3) [56] are found in the IR-spectrum corresponding to mostly b-type substituted carbonate hydroxyapatite, where carbonate occupies phosphate lattice sites in the HAP structure [57,58] (Fig. 5**IV**). XRD patterns (Fig. 5**III**) display a pure crystalline HAP phase according to PDF# 01-074-0565 in the case of the SE whatever is the temperature. This is the reason why SE is referred to as the optimized solution. Finally, from these results, one can assume the existence of a thermal barrier of about 325 °C for a substrate temperature, above which a constant value of the Ca/P molar ratio is reached for both solutions (Fig. 2). To summarize, the conditions for obtaining a coating of pure hydroxyapatite must operate under a nominal Ca/P molar ratio less than or equal to 0.8, and at a substrate temperature higher than 325 ° C, to compensate for the evaporation of the TEP in EtOH and favor its reactivity.

4.2. Microstructure and structure control of HAP-coatings

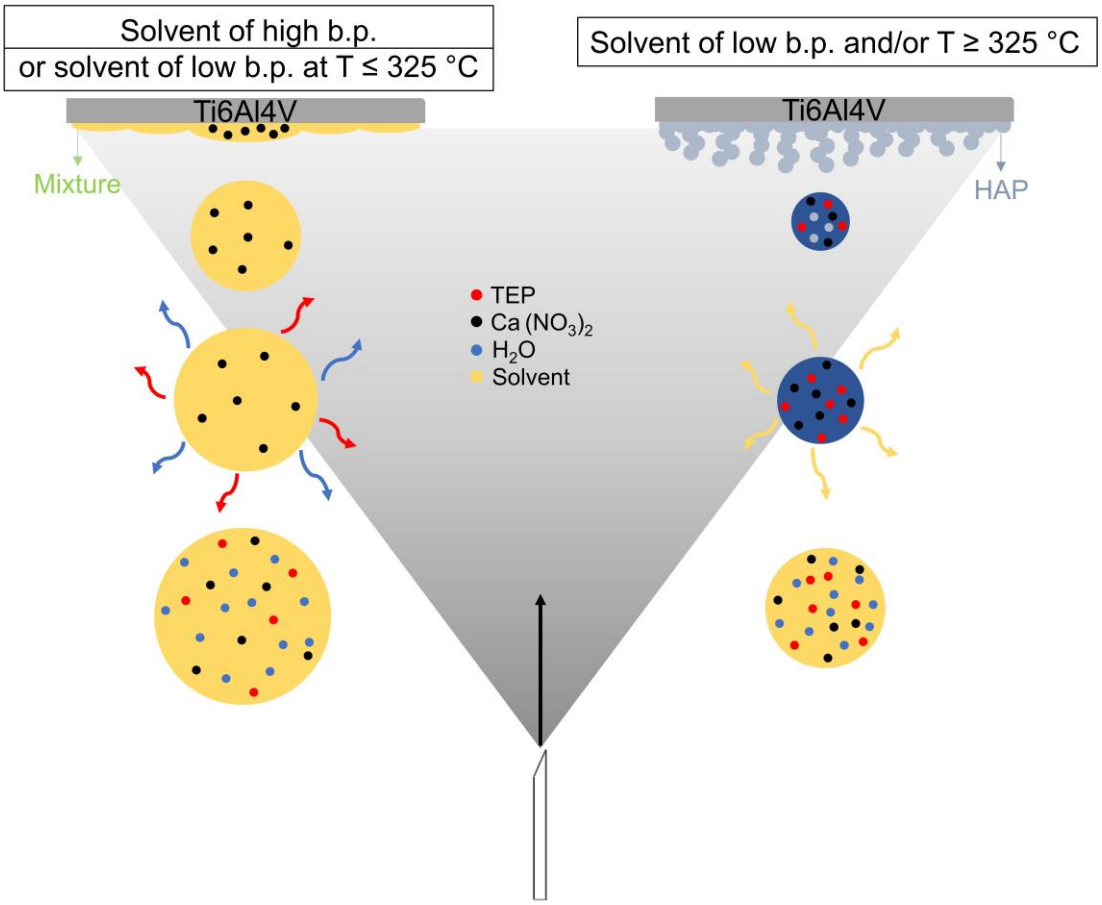

Fig. 9. Sketch representing the two extreme situations under electrospraying of the precursor solution. On the left side, complete loss of TEP and H2O occurs due to a low substrate temperature (lower than 325 °C) or the use of a solvent of high boiling point. On the right side, the reagents are not lost during the deposition process, and HAP precipitation occurs.

One of the main advantages of ESD is the precise mastery of the coating morphology as a function of the substrate temperature and/or the boiling point of the solvent [29,59,60]. According to the droplet size impacting the substrate, two extreme cases can be considered, as represented in the sketch in Fig. 9. As shown previously, the droplet size is mainly dependent on the boiling point of the solvents but also on the electrical conductivity of the solution according to Gañan-Calvo's equation (Equation 1), in addition to the ESD deposition conditions and especially to the substrate temperature. When a low substrate temperature is used, such as 300 °C, large droplets retain enough liquid to simultaneously spread and dry on the substrate surface, leading to the formation of dense-type films (Fig. 3**II**). This dense morphology can be also obtained with large droplets containing large solvent content of high boiling point, like BC, whatever the temperature, 300 °C or 350 °C (Fig. 3**V** and Fig. 3**VI**). In contrast, when the droplets contain a solvent of low boiling point, severe droplet drying takes place during the droplet flight between the nozzle and the heated substrate. For a higher substrate temperature (≥ 325 °C), the droplets impacting the substrate are almost or entirely dried. Solid particles are formed and impact the substrate, forming protrusions on the surface. Due to electrostatic attraction, the next charged particles will preferentially land on the top of the pronounced curvatures on the substrate [51,61]. This leads to the preferential landing effect (Fig. 3**I**). A coral-type, highly porous microstructure is produced. This

morphology of HAP coatings is the most prevalent one since a substrate temperature above 325 °C is required to favor the TEP reactivity, and solvents of a low boiling point are preferable to avoid the TEP evaporation.

When solutions with a low Ca/P molar ratio (high TEP concentration) are used, the average crystallite size of as-deposited HAP coatings decreases, as observed in XRD patterns (Fig. 2**I**). Indeed, it has been found to decrease from 33 ± 3 nm to 16 ± 4 nm when the TEP concentration was passing from 9 to 75 mM TEP (Table S1, SA and SH, respectively). This phenomenon might occur because a large phosphorus concentration probably enhances the nucleation rate of HAP over crystal growth during the deposition [62,63]. This tendency towards smaller grain size by managing the Ca/P molar ratio of the precursor solution has been never reported before and requires further study. Since it opens the possibility to precisely control the dissolution rate of HAP coatings in a biological medium by tailoring its crystallite size. The deposition of a multi-layer coating could be envisaged with a gradient of crystallinity, composed of a very thin well-attached crystalline HAP layer close to the substrate becoming more amorphous at the surface of the coating.

The role of post-deposition heat treatment on the as-deposited films can be discussed in terms of phases, morphology, and crystallite size versus a slow and fast heating rate. Slow heat-treatment up to 800 °C leads to the formation of rutile and traces of anatase (Fig. 6**I**) and is often associated with the delamination of the coating. The film is expected to undergo too large mechanical stresses since the metallic substrate and the CaP coating present different thermal expansion coefficients, i. e., Ti6Al4V = 9×10^{-6} K^{-1} and HAP = 13.3×10^{-6} K^{-1} [19,64]. Consequently, cracking and delamination occur. Fast heat treatment of as-deposited coatings up to 700 °C, starting from solutions SA and SE, has proven to avoid Ti-substrate oxidation and substrate diffusion in the coating, as shown from XRD analysis (Fig. 6**II**). Once the Ca/P molar ratio in the solution is optimized (SE), no formation of a secondary phase, $CaCO_3$, or/and CaO is observed in the fast heat-treated coatings (Fig. 6**II** (a)). This demonstrates, once again, the phase purity reached by this method. It is worth mentioning that no alteration of microstructure occurs in pure 3D-coral-type HAP coatings before and after a fast heat treatment at 700 °C, as shown by SEM observations (Fig. S1). Besides, a similar increase in grain size is observed at all heating-rates. While crystal growth is a thermally activated phenomenon, nano-structuring is maintained in these conditions. It is concluded that a fast heat-treatment is preferable to a conventional one to avoid oxidation of the substrate. Indeed, the stability of the microstructure and chemical composition of the coatings are of great interest since it was demonstrated that heat treatment could improve adhesion between the metal implant and the coating, which is crucial in the long-term stability of the implant.

5. Conclusions

This work reports the fabrication of single-phase HAP coatings on Ti6Al4V substrate, in one-step by a versatile and low-cost method, the ESD process, starting from an alcoholic solution of $Ca(NO_3)_2$ and TEP as the Ca(II) and P(V) precursors respectively. Porous 3D coral-type and dense morphologies of CaP coatings were successfully obtained for selected substrate temperatures and precursor solutions. During the ESD deposition, two main processes, evaporation and hydrolysis of the precursors, take place in combination with the decomposition of the solution of precursors and the spreading/drying of the droplets when they impact the hot substrate. The measured Ca/P molar ratio, different from the nominal value, was found to be homogeneous in the films and is dependent on the precursor concentration, nature of solvents, and the substrate temperature. Single-phase nanostructured HAP coatings, 30 nm in crystallite size, were obtained by electrospraying an optimized solution (SE: 15mM $Ca(NO_3)_2$ and 18.75 mM TEP dissolved in ethanol, nominal Ca/P molar ratio of 0.8) at 350 °C for 1.5 h under 6 - 7 kV, for a fixed nozzle-to-substrate distance of 30 mm and a flow-rate of 1.5 mL h^{-1}. The final Ca/P molar ratio and the microstructure are independent of a post-ESD thermal treatment, whatever the heating rate. When a fast heat treatment is performed on optimized films, the HAP remains a single phase. This fast annealing process is preferred to a conventional one since it prevents the oxidation of the Ti6Al4V substrate and the diffusion of the metallic alloy into the ESD coating while preserving the morphology and the structure of the film.

Acknowledgments

The authors would like to thank T. Encinas for XRD support and F. Charlot for SEM and EDS analyses in CMTC (Grenoble INP, France). ED and MJ thank Grenoble INP and UGA for funding the hosting of foreign scientists.

This research was supported by the French National Agency of Research in a DECaP Project ANR-17-CE19-0004.

References

[1] J. Huang, S.M. Best, W. Bonfield, R.A. Brooks, N. Rushton, S.N. Jayasinghe, M.J. Edirisinghe, In vitro assessment of the biological response to nano-sized hydroxyapatite, J. Mater. Sci. Mater. Med. 15 (2004) 441–445. https://doi.org/10.1023/B:JMSM.0000021117.67205.cf.

[2] M. Metikoš-Huković, E. Tkalacec, A. Kwokal, J. Piljac, An in vitro study of Ti and Ti-alloys coated with sol-gel derived hydroxyapatite coatings, Surf. Coatings Technol. 165 (2003) 40–50. https://doi.org/10.1016/S0257-8972(02)00732-6.

[3] W.J.A. Dhert, C.P.A.T. Klein, J.A. Jansen, E.A. van der Velde, R.C. Vriesde, P.M. Rozing, K. de Groot, A histological and histomorphometrical investigation of fluorapatite, magnesiumwhitlockite, and hydroxylapatite plasma-sprayed coatings in goats, J. Biomed. Mater. Res. 27 (1993) 127–138. https://doi.org/10.1002/jbm.820270116.

[4] F. Barrère, C.M. Van Der Valk, G. Meijer, R.A.J. Dalmeijer, K. De Groot, P. Layrolle, Osteointegration of Biomimetic Apatite Coating Applied onto Dense and Porous Metal Implants in Femurs of Goats, J. Biomed. Mater. Res. - Part B Appl. Biomater. 67 (2003) 655–665. https://doi.org/10.1002/jbm.b.10057.

[5] M.J. Dalby, L. Di Silvio, E.J. Harper, W. Bonfield, Initial interaction of osteoblasts with the surface of a hydroxyapatite-poly(methylmethacrylate) cement, Biomaterials. 22 (2001) 1739–1747. https://doi.org/10.1016/S0142-9612(00)00334-3.
[6] L.L. Hench, J. Wilson, W.R. Lacefield, Hydroxylapatite coatings, in: An Introd. to Bioceram., 1993. https://doi.org/10.1142/9789814317351_0012.
[7] R.Z. LeGeros, Biodegradation and bioresorption of calcium phosphate ceramics, Clin. Mater. 14 (1993) 65–88. https://doi.org/10.1016/0267-6605(93)90049-D.
[8] Y. Cai, R. Tang, Calcium phosphate nanoparticles in biomineralization and biomaterials, J. Mater. Chem. 18 (2008) 3775–3787. https://doi.org/10.1039/b805407j.
[9] V.P. Orlovskii, V.S. Komlev, S.M. Barinov, Hydroxyapatite and hydroxyapatite-based ceramics, Inorg. Mater. 38 (2002) 973–984. https://doi.org/10.1023/A:1020585800572.
[10] J.D. Pasteris, B. Wopenka, E. Valsami-Jones, Bone and tooth mineralization: Why apatite?, Elements. 4 (2008) 97–104. https://doi.org/10.2113/GSELEMENTS.4.2.97.
[11] A.A. Campbell, Bioceramics for implant coatings, Mater. Today. 6 (2003) 26–30. https://doi.org/10.1016/S1369-7021(03)01128-3.
[12] A. Sun, L., Berndt, C. C., Gross, K. A., & Kucuk, Material fundamentals and clinical performance of APS HP coatings Review, (2001).
[13] Herbert Herman, Plasma spray deposition processes, MRS Bull. 12 (1988) 60–67.
[14] V. Pálka, E. Poštrková, H.K. Koerten, Some characteristics of hydroxylapatite powder particles after plasma spraying, Biomaterials. 19 (1998) 1763–1772. https://doi.org/10.1016/S0142-9612(98)00087-8.
[15] O. Graßmann, R.B. Heimann, Compositional and microstructural changes of engineered plasma-sprayed hydroxyapatite coatings on Ti6Al4V substrates during incubation in protein-free simulated body fluid, J. Biomed. Mater. Res. 53 (2000) 685–693. https://doi.org/10.1002/1097-4636(2000)53:6<685::AID-JBM11>3.0.CO;2-B.
[16] M.T. Carayon, J.L. Lacout, Study of the Ca/P atomic ratio of the amorphous phase in plasma-sprayed hydroxyapatite coatings, J. Solid State Chem. 172 (2003) 339–350. https://doi.org/10.1016/S0022-4596(02)00085-3.
[17] J. Chen, W. Tong, Y. Cao, J. Feng, X. Zhang, Effect of atmosphere on phase transformation in plasma-sprayed hydroxyapatite coatings during heat treatment, J. Biomed. Mater. Res. 34 (1997) 15–20. https://doi.org/10.1002/(SICI)1097-4636(199701)34:1<15::AID-JBM3>3.0.CO;2-Q.
[18] E. Mohseni, E. Zalnezhad, A.R. Bushroa, Comparative investigation on the adhesion of hydroxyapatite coating on Ti-6Al-4V implant: A review paper, Int. J. Adhes. Adhes. 48 (2014) 238–257. https://doi.org/10.1016/j.ijadhadh.2013.09.030.
[19] Y.C. Tsui, C. Doyle, T.W. Clyne, Plasma sprayed hydroxyapatite coatings on titanium substrates. Part 1: Mechanical properties and residual stress levels, Biomaterials. 19 (1998) 2015–2029. https://doi.org/10.1016/S0142-9612(98)00103-3.
[20] B.C. Wang, T.M. Lee, E. Chang, C.Y. Yang, The shear strength and the failure mode of plasma-sprayed hydroxyapatite coating to bone: The effect of coating thickness, J. Biomed. Mater. Res. 27 (1993) 1315–1327. https://doi.org/10.1002/jbm.820271012.
[21] C.Y. Yang, B.C. Wang, T.M. Lee, E. Chang, G.L. Chang, Intramedullary implant of plasma-sprayed hydroxyapatite coating: An interface study, J. Biomed. Mater. Res. 36 (1997) 39–48. https://doi.org/10.1002/(SICI)1097-4636(199707)36:1<39::AID-JBM5>3.0.CO;2-M.
[22] A.K. Lynn, D.L. DuQuesnay, Hydroxyapatite-coated Ti–6Al–4V, Biomaterials. 23 (2002) 1937–1946. https://doi.org/10.1016/s0142-9612(01)00321-0.
[23] C. Domínguez-Trujillo, E. Peón, E. Chicardi, H. Pérez, J.A. Rodríguez-Ortiz, J.J. Pavón, J. García-Couce, J.C. Galván, F. García-Moreno, Y. Torres, Sol-gel deposition of hydroxyapatite

coatings on porous titanium for biomedical applications, Surf. Coatings Technol. 333 (2018) 158–162. https://doi.org/10.1016/j.surfcoat.2017.10.079.
[24] M. Łukaszewska-Kuska, P. Krawczyk, A. Martyla, W. Hędzelek, B. Dorocka-Bobkowska, Hydroxyapatite coating on titanium endosseous implants for improved osseointegration: Physical and chemical considerations, Adv. Clin. Exp. Med. 27 (2018) 1055–1059. https://doi.org/10.17219/acem/69084.
[25] R.I.M. Asri, W.S.W. Harun, M.A. Hassan, S.A.C. Ghani, Z. Buyong, A review of hydroxyapatite-based coating techniques: Sol-gel and electrochemical depositions on biocompatible metals, J. Mech. Behav. Biomed. Mater. 57 (2016) 95–108. https://doi.org/10.1016/j.jmbbm.2015.11.031.
[26] R.A. Surmenev, A review of plasma-assisted methods for calcium phosphate-based coatings fabrication, Surf. Coatings Technol. 206 (2012) 2035–2056. https://doi.org/10.1016/j.surfcoat.2011.11.002.
[27] V. Nelea, C. Morosanu, M. Iliescu, I.N. Mihailescu, Microstructure and mechanical properties of hydroxyapatite thin films grown by RF magnetron sputtering, Surf. Coatings Technol. 173 (2003) 315–322. https://doi.org/10.1016/S0257-8972(03)00729-1.
[28] G.C. Gomes, F.F. Borghi, R.O. Ospina, E.O. López, F.O. Borges, A. Mello, Nd:YAG (532 nm) pulsed laser deposition produces crystalline hydroxyapatite thin coatings at room temperature, Surf. Coatings Technol. 329 (2017) 174–183. https://doi.org/10.1016/j.surfcoat.2017.09.008.
[29] H. Herø, H. Wie, R.B. Jørgensen, I.E. Ruyter, Hydroxyapatite coatings on Ti produced by hot isostatic pressing, J. Biomed. Mater. Res. 28 (1994) 343–348. https://doi.org/10.1002/jbm.820280308.
[30] M.A. Auger, B. Savoini, A. Muñoz, T. Leguey, M.A. Monge, R. Pareja, J. Victoria, Mechanical characteristics of porous hydroxyapatite/oxide composites produced by post-sintering hot isostatic pressing, Ceram. Int. 35 (2009) 2373–2380. https://doi.org/10.1016/j.ceramint.2009.01.016.
[31] S. Leeuwenburgh, J. Wolke, J. Schoonman, J. Jansen, Electrostatic spray deposition (ESD) of calcium phosphate coatings, J. Biomed. Mater. Res. - Part A. 66 (2003) 330–334. https://doi.org/10.1002/jbm.a.10590.
[32] S.C.G. Leeuwenburgh, J.G.C. Wolke, M.C. Siebers, J. Schoonman, J.A. Jansen, In vitro and in vivo reactivity of porous, electrosprayed calcium phosphate coatings, Biomaterials. 27 (2006) 3368–3378. https://doi.org/10.1016/j.biomaterials.2006.01.052.
[33] S.C.G. Leeuwenburgh, J.G.C. Wolke, L. Lommen, T. Pooters, J. Schoonman, J.A. Jansen, Mechanical properties of porous, electrosprayed calcium phosphate coatings, J. Biomed. Mater. Res. - Part A. 78 (2006). https://doi.org/10.1002/jbm.a.30770.
[34] W.H. Lee, Y.H. Kim, N.H. Oh, Y.W. Cheon, Y.J. Cho, C.M. Lee, K.B. Kim, N.S. Lee, A Study of Hydroxyapatite Coating on Porous Ti Compact by Electrostatic Spray Deposition, Solid State Phenom. 124–126 (2007) 1789–1792. https://doi.org/10.4028/www.scientific.net/ssp.124-126.1789.
[35] S. Singh, V.K. Meena, M. Sharma, H. Singh, Preparation and coating of nano-ceramic on orthopaedic implant material using electrostatic spray deposition, Mater. Des. 88 (2015) 278–286. https://doi.org/10.1016/j.matdes.2015.08.145.
[36] W. Jiang, L. Sun, G. Nyandoto, A.P. Malshe, Electrostatic spray deposition of nanostructured hydroxyapatite coating for biomedical applications, J. Manuf. Sci. Eng. Trans. ASME. 130 (2008) 0210011–0210017. https://doi.org/10.1115/1.2816016.
[37] M. Iafisco, R. Bosco, S.C.G. Leeuwenburgh, J.J.J.P. Van Den Beucken, J.A. Jansen, M. Prat, N. Roveri, Electrostatic spray deposition of biomimetic nanocrystalline apatite coatings onto titanium, Adv. Eng. Mater. 14 (2012) 13–20. https://doi.org/10.1002/adem.201180062.

[38] D. Marinha, L. Dessemond, E. Djurado, Comprehensive Review of Current Developments in IT-SOFCs, Curr. Inorg. Chem. 3 (2013) 2–22. https://doi.org/10.2174/1877944111303010003.
[39] A.M. Gañán-Calvo, J. Dávila, A. Barrero, Current and droplet size in the electrospraying of liquids. Scaling laws, J. Aerosol Sci. 28 (1997) 249–275. https://doi.org/10.1016/S0021-8502(96)00433-8.
[40] D.R. Lide, CRC Handbook of Chemistry and Physics 86TH Edition 2005-2006, 2005.
[41] O. Wilhelm, L. Mädler, S.E. Pratsinis, Electrospray evaporation and deposition, J. Aerosol Sci. 34 (2003) 815–836. https://doi.org/10.1016/S0021-8502(03)00034-X.
[42] J.F. de la Mora, I.G. Loscertales, The current emitted by highly conducting Taylor cones, J. Fluid Mech. 260 (1994) 155–184. https://doi.org/10.1017/S0022112094003472.
[43] G.I. Taylor, Disintegration of water drops in an electric field, Proc. R. Soc. A. 280 (1964) 383–397. http://rspa.royalsocietypublishing.org/content/royprsa/280/1382/383.full.pdf.
[44] A.X. Analysis, V.C.R. Hubbard, C.S. Barrett, P.K. Predecki, D.E. Leyden, Advances in X-ray Analysis, 1982.
[45] S.N. Danilchenko, O.G. Kukharenko, C. Moseke, I.Y. Protsenko, L.F. Sukhodub, B. Sulkio-Cleff, Determination of the bone mineral crystallite size and lattice strain from diffraction line broadening, Cryst. Res. Technol. 37 (2002) 1234–1240. https://doi.org/10.1002/1521-4079(200211)37:11<1234::AID-CRAT1234>3.0.CO;2-X.
[46] S. Joschek, B. Nies, R. Krotz, A. Göpferich, Chemical and physicochemical characterization of porous hydroxyapatite ceramics made of natural bone, Biomaterials. 21 (2000) 1645–1658. https://doi.org/10.1016/S0142-9612(00)00036-3.
[47] M. Wei, J.H. Evans, T. Bostrom, L. GrØndahl, Synthesis and characterization of hydroxyapatite, fluoride-substituted hydroxyapatite and fluorapatite, J. Mater. Sci. Mater. Med. 14 (2003) 311–320. https://doi.org/10.1023/A:1022975730730.
[48] R. Cuscó, F. Guitián, A. De Aza, L. Artús, Differentiation between hydroxyapatite and β-tricalcium phosphate by means of μ-Raman spectroscopy, J. Eur. Ceram. Soc. 18 (1998) 1301–1305. https://doi.org/10.1016/s0955-2219(98)00057-0.
[49] W.M. Haynes, CRC Handbook Chemistry and Physics, CRC Press. (2016).
[50] E. Park, R.A. Condrate, D. Lee, Infrared spectral investigation of plasma spray coated hydroxyapatite, Mater. Lett. 36 (1998) 38–43. https://doi.org/10.1016/S0167-577X(97)00287-5.
[51] C.H. Chen, M.H.J. Emond, E.M. Kelder, B. Meester, J. Schoonman, Electrostatic sol-spray deposition of nanostructured ceramic thin films, J. Aerosol Sci. 30 (1999) 959–967. https://doi.org/10.1016/S0021-8502(98)00075-5.
[52] J.R. Cox, O.B. Ramsay, Mechanisms of nucleophilic substitution in phosphate esters, Chem. Rev. 64 (1964) 317–352. https://doi.org/10.1021/cr60230a001.
[53] S. Shi, S. Chen, X. Zhang, W. Shen, X. Li, W. Hu, H. Wang, Biomimetic mineralization synthesis of calcium-deficient carbonate-containing hydroxyapatite in a three-dimensional network of bacterial cellulose, J. Chem. Technol. Biotechnol. 84 (2009) 285–290. https://doi.org/10.1002/jctb.2037.
[54] J.P. Lafon, E. Champion, D. Bernache-Assollant, Processing of AB-type carbonated hydroxyapatite Ca10-x(PO4)6-x(CO3)x(OH)2-x-2y(CO3)y ceramics with controlled composition, J. Eur. Ceram. Soc. 28 (2008) 139–147. https://doi.org/10.1016/j.jeurceramsoc.2007.06.009.
[55] S.C.G. Leeuwenburgh, J.G.C. Wolke, J. Schoonman, J.A. Jansen, Influence of precursor solution parameters on chemical properties of calcium phosphate coatings prepared using Electrostatic Spray Deposition (ESD), Biomaterials. 25 (2004) 641–649. https://doi.org/10.1016/S0142-9612(03)00575-1.
[56] S. Koutsopoulos, Synthesis and characterization of hydroxyapatite crystals: A review study on

the analytical methods, J. Biomed. Mater. Res. 62 (2002) 600–612. https://doi.org/10.1002/jbm.10280.
[57] H. El Feki, C. Rey, M. Vignoles, Carbonate ions in apatites: Infrared investigations in the v4 CO3 domain, Calcif. Tissue Int. 49 (1991) 269–274. https://doi.org/10.1007/BF02556216.
[58] H. Chihi, I. Khattech, M. Jemal, Preparation, characterization and thermochemistry of magnesium carbonate co-substituted fluorapatites, J. Therm. Anal. Calorim. 127 (2017) 2427–2438. https://doi.org/10.1007/s10973-016-5693-2.
[59] R.K. Sharma, E. Djurado, An efficient hierarchical nanostructured Pr6O11 electrode for solid oxide fuel cells, J. Mater. Chem. A. 6 (2018) 10787–10802. https://doi.org/10.1039/c8ta00190a.
[60] E. Djurado, A. Salaün, G. Mignardi, A. Rolle, M. Burriel, S. Daviero-Minaud, R.N. Vannier, Electrostatic spray deposition of Ca3Co4O9 + δ layers to be used as cathode materials for IT-SOFC, Solid State Ionics. 286 (2016) 102–110. https://doi.org/10.1016/j.ssi.2016.01.021.
[61] A. Lintanf, A. Mantoux, E. Blanquet, E. Djurado, Elaboration of Ta2O5 thin films using electrostatic spray deposition for microelectronic applications, J. Phys. Chem. C. 111 (2007) 5708–5714. https://doi.org/10.1021/jp0676585.
[62] G. Galster, K.F. Nielsen, Crystal Growth From Solution., Eur. Sp. Agency, (Special Publ. ESA SP. (1984) 189–191.
[63] I.H. Leubner, A balanced nucleation and growth model for controlled precipitations, J. Dispers. Sci. Technol. 22 (2001) 125–138. https://doi.org/10.1081/DIS-100102688.
[64] H. Li, K.A. Khor, P. Cheang, Thermal sprayed hydroxyapatite splats: Nanostructures, pore formation mechanisms and TEM characterization, Biomaterials. 25 (2004) 3463–3471. https://doi.org/10.1016/j.biomaterials.2003.10.051.

Supplementary material

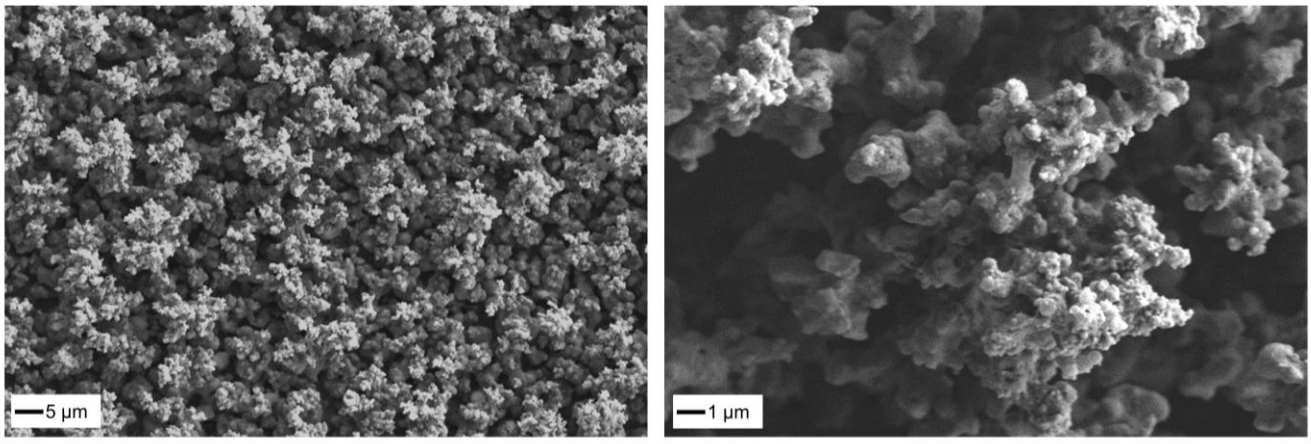

Fig. S1. SEM surface views of single phased HAP coating on Ti6Al4V after heat treatment at 700 °C for 15 min under IR lamp. The ESD coating was deposited with the SE optimized precursor solution (15 mM $Ca(NO_3)_2$, and 18.75 mM TEP in pure ethanol, Ca/P = 0.8), at 350 °C for a needle-to-substrate distance of 30 mm, a flow rate of 1.5 ml h^{-1} and a deposition time of 1.5 h.

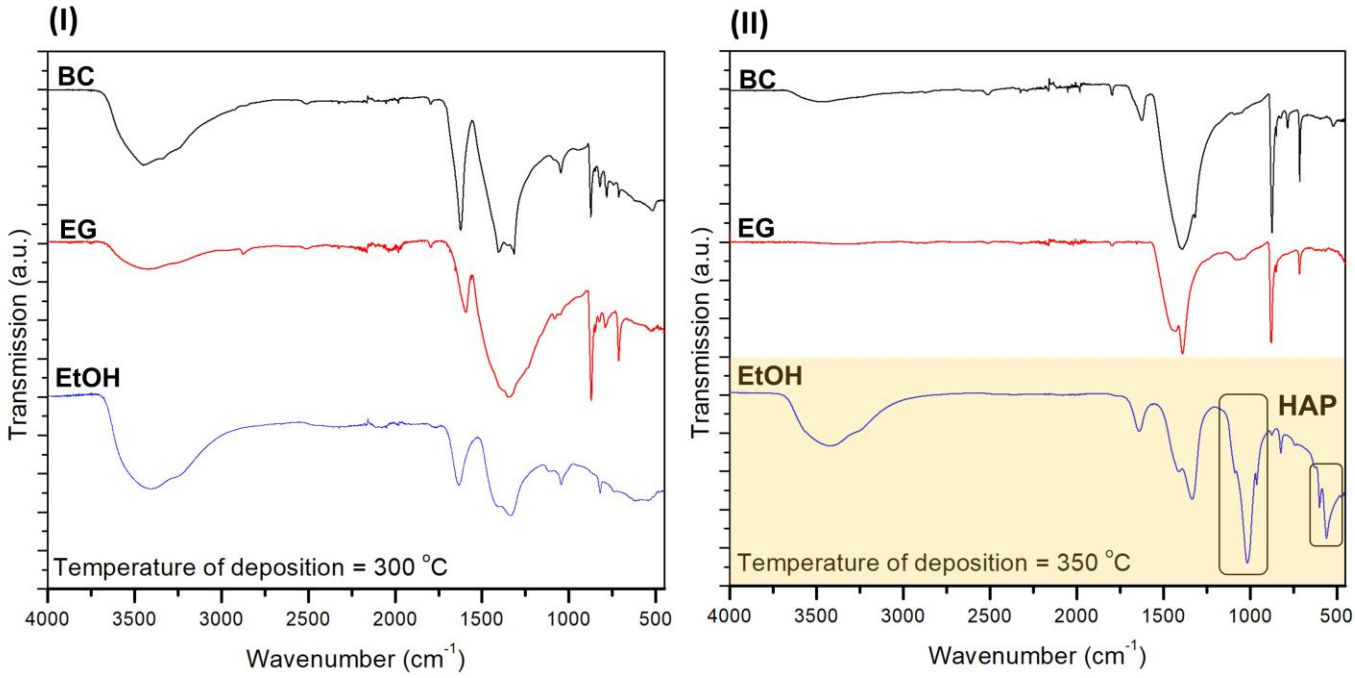

*Fig. S2. FTIR spectra of as-deposited coatings by ESD at **(I)** 300 °C and **(II)** 350 °C for different solvents using a nominal composition of 15 mM $Ca(NO_3)_2$, and 9 mM TEP, Ca/P = 1.67, with a needle-to-substrate distance of 30 mm, a flow rate of 1.5 ml h^{-1}, and a deposition time of 1.5 h.*

*Table S1. Calculated average crystallite size from XRD patterns presented in this work and main ESD process parameters employed; TEP nominal concentration, nature of the solvent(s), substrate temperature (T), nominal Ca/P ratio of precursor solutions, and calculated crystallite size. The nominal concentration of Ca(NO3)2 was 15 mM for all solutions. Deposition time (t) was fixed at 1.5 h, needle-to-substrate distance (d) at 30 mm, and flow rate (Q) at 1.5 mL h-1. Calculated crystallite size: #after conventional heat-treatment (HT) in a furnace at a heating rate of 15 °C min-1 for 60 min. up to 700 °C; *after fast HT under an infrared lamp at a heating rate of 300 °C min-1 for 15 min up to 700 °C.*

TEP (mM)	Nature of solvent(s)	T (°C)	Nominal Ca/P ratio	Crystallite size (nm)
9	EtOH	325	1.67	31 ± 4
18.75	EtOH	325	0.8	23 ± 3
9	EtOH	350	1.67	34 ± 3
-	-	-	-	52 ± 2#
-	-	-	-	49 ± 4*
18.75	EtOH	350	0.8	30 ± 4
-	-	-	-	50 ± 3#
-	-	-	-	48 ± 3*
25	EtOH	350	0.6	25 ± 3
37.5	EtOH	350	0.4	22 ± 4
75	EtOH	350	0.2	16 ± 3
9	EtOH	375	1.67	39 ± 3
18.75	EtOH	375	0.8	34 ± 3
9	EtOH	400	1.67	43 ± 3
18.75	EtOH	400	0.8	39 ± 3